Physics of Fluids

A thorough experimental investigation on airfoil turbulence interaction noise

Cite as: Phys. Fluids **35**, 035123 (2023); https://doi.org/10.1063/5.0142704
Submitted: 16 January 2023 • Accepted: 27 February 2023 • Accepted Manuscript Online: 28 February 2023 • Published Online: 16 March 2023
Published open access through an agreement with JISC Collections

L. Bowen, A. Celik and M. Azarpeyvand

Physics of Fluids ARTICLE scitation.org/journal/phf

A thorough experimental investigation on airfoil turbulence interaction noise

Cite as: Phys. Fluids **35**, 035123 (2023); doi: 10.1063/5.0142704
Submitted: 16 January 2023 · Accepted: 27 February 2023 ·
Published Online: 16 March 2023

L. Bowen,[1,a)] A. Celik,[2] and M. Azarpeyvand[1]

AFFILIATIONS

[1]Faculty of Engineering, University of Bristol, Bristol BS8 1TR, United Kingdom
[2]Aerospace Engineering, Swansea University, Swansea SA1 8EN, United Kingdom

[a)]Author to whom correspondence should be addressed: luke.bowen@bristol.ac.uk

ABSTRACT

This paper on airfoil turbulence interaction noise reveals the nature of the relation between the distortion type of turbulent structures and radiated far-field noise. The turbulence interaction phenomenon is explored through comprehensive simultaneous hot-wire, surface pressure, and far-field noise measurements. Two grid turbulence cases are utilized to examine the effect of the coherent structure's length scale compared to the airfoil's leading-edge radius. The results show that the turbulent structures with a size comparable to the leading-edge radius disperse into smaller three-dimensional structures, losing their spatial coherence in the vicinity of the stagnation point. In contrast, the structures with larger integral length scales distort into highly coherent two-dimensional structures, yielding an increase in the surface pressure fluctuation energy spectra and the chordwise extent of the affected area by the interaction phenomenon, which is found to be responsible for the increased levels of far-field noise. The turbulence characteristics of the flow far upstream of the stagnation point determine the unsteady loading behavior at the stagnation point yet have little influence on the unsteady loading of the full airfoil chord. The stagnation point velocity fluctuations manifest a strong link to the remainder of the airfoil chord, as well as the near-field hydrodynamic to far-field acoustic signal coherence, while demonstrating no communication with the surface pressure fluctuations at the stagnation point.

I. INTRODUCTION

Noise generated by a turbulent flow interacting with a lifting body is an important societal concern. This noise mechanism is generated by a host of everyday items, from turbofan engines to household appliances. In most applications, a turbulent flow is generated, which interacts with a body. In certain instances, the interaction can be an effective noise generation mechanism. The efficiency of this noise generation depends on the ratio between the length scale of the turbulence structures and the leading edge radius with which it interacts.

The generation of a turbulent flow in a controlled environment, such as a wind tunnel, was first proposed in the inaugural works of Simmons *et al.*[1] and has sustained serious interest since.[2–7] Generally, a grid of round or square rods is employed to disturb the smooth flow, that is, characteristic of wind tunnel facilities. A simple, passive turbulence generating grid can generate homogeneous, nearly isotropic turbulence within ten mesh lengths downstream of the grid.[5] To improve the isotropy, a small axisymmetric contraction is employed, which strains the turbulent fluctuations so that each velocity fluctuation component becomes equal.[3] More recently, research on turbulence generation in aeroacoustic facilities has gathered attraction due to societal concern of turbulence interaction noise. Geyer *et al.*[8] linked the pressure drop across nets and screens to the self-noise generated by the grid and created a prediction tool for noise generated by nets or screens. Bowen *et al.*[7] studied the effect of grid geometry and associated flow properties on grid self-noise, in addition to turbulence interaction noise with case studies involving airfoil and cylinder models.

The interaction of a turbulent flow with a body has undergone significant research to date and is comprehensively reviewed by Mish and Devenport.[9] Two main areas of research are the airfoil response to the turbulent flow and the effect of the turbulent flow impinging on a body. Initially, analytical models were developed with the concept of the body modeled as a flat plate at zero angle of attack, stemming from the works of Von Kármán and Sears[10] and Sears.[11] These initial works are based on incompressible flow assumption where a sinusoidal upwash gust interacts with a flat plate. This was further developed by a host of researchers to include compressibility effects to have the interaction of a compressible skewed gust response,[12,13] compressible two-dimensional gust response,[14,15] and then to have compressible skewed

non-convected gust response.[16–18] To include the effects of airfoil geometry and angle of attack, analytical models are required to account for the distortion of the incoming gust due to the airfoil body. Rapid distortion theory (RDT) is the basis for this analysis, which was introduced by Hunt,[19] It is a method for calculating the turbulent velocity around a bluff body upstream of areas of detached flow, based on specific conditions relating to the integral length scale of the turbulent structures to the radius of the bluff body. Goldstein and Atassi,[20] along with McKeough[21] and Mckeough and Graham,[22] utilized the RDT to calculate the airfoil response.

A common goal of turbulence interaction noise research is to develop theoretical and empirical models from the airfoil response to turbulent gust to utilize as prediction tools. The previous research into the noise generated due to turbulence interaction with a solid body is stemmed from Curle and Lighthill[23] acoustic analogy, which proposes the source of the aerodynamic noise as the unsteady pressure fluctuations on the airfoil for a compact source. The pressure fluctuations result from the interaction of the solid airfoil surface with the incoming turbulent flow in low Mach number flows. Perhaps the most influential model for the prediction of turbulent interaction noise is that of Amiet,[18] in which linearized airfoil theory is utilized to calculate the aerodynamic response from an incident gust, then accounting for scattering effects and the mean flow of the unsteady lift is propagated to the acoustic far-field. Specifically, the spanwise correlation of the vortical structures and the integral length scale of the upwash velocity fluctuations are vital to the noise prediction. Paterson and Amiet[24] showed that thoroughly characterizing the turbulent inflow allows the prediction of turbulence interaction noise by an experimental study, where the surface pressure fluctuations and far-field noise were measured for a NACA 0012 airfoil and compared to the analytical model.

The dominant noise source of an airfoil in a turbulent flow is the impingement on the leading edge, provided the level of turbulence intensity is sufficient.[25] Until recently, several studies have sought to improve the prediction of turbulence interaction noise with extensions of Amiet's theory or further experimental investigation. Gershfeld[26] studied the noise from thick airfoils in turbulent flows and demonstrated attenuation in the power spectrum of the noise due to airfoil thickness, relating the reduction to the product of the convection wavenumber and half the airfoils maximum thickness. Observations made by Moreau and Roger[27] reported the effect of angle of attack and airfoil shape on the turbulence interaction noise. Their study reported a slight effect to the far-field noise with changing the angle of attack but observed airfoil thickness having a substantial consequence of the far-field noise, i.e., a 10 dB reduction when the thickness of the airfoil exceeds the integral length scale of the turbulence. Devenport *et al.*[28] also observed the sensitivity of the far-field noise in isotropic turbulence to limited angle of attack. Specifically, Devenport *et al.*[28] observed a significant sensitivity to the airfoil response function due to the distortion of the flow. However, the distortion effects are neutralized by the averaging of the response function due to the isotropic turbulence energy spectrum. Provided calculations for a NACA 0015 airfoil show a significant increase in turbulence interaction noise with an increasing angle of attack in anisotropic turbulence. The low sensitivity to angle of attack that was previously observed was corroborated in an experimental study by Celik *et al.*,[29] which also demonstrates the low sensitivity to angle of attack extends to the lift and drag spectra too.

The turbulent inflow conditions have been identified as an important factor by Amiet for noise generation and were extensively studied by Hutcheson *et al.*[30] In an experimental study, variations to the inflow conditions and geometries demonstrated that the noise generation increases as the length scale and the turbulence intensity increase. In recent studies, the airfoil geometry has been identified and addressed as an important factor in noise generation.[26–28,31] Comparatively, Bowen *et al.*[7] observed significant changes to the turbulence interaction noise in the experimental study performed with a NACA0012 airfoil immersed in twelve different turbulent flows of varying turbulence intensity and integral length scale. Furthermore, rapid distortion theory has been utilized for the improvement of noise prediction of airfoil-turbulence interaction where Christophe,[32] Santana *et al.*,[33] and Zamponi *et al.*[34] demonstrated the sensitivity of the ratio between the leading edge radius and integral length scales of the flow. More recently, turbulence interaction noise has been the subject of noise reduction studies through the use of flow control techniques. Serrations[35–39] and porous materials[34,40–46] in various configurations have been effectively implemented to reduce turbulence interaction noise. However, there still lacks physical observation of the mechanisms in turbulence interaction noise and how it is reduced using flow control devices.

This experimental study aims at reporting the observed turbulence interaction noise in multiple turbulent flows in conjunction with the in-depth assessment of the turbulent velocity field, airfoil response, and their link. The manuscript demonstrates how the turbulence intensity and integral length scale of the turbulence structures can affect the far-field noise through the distortion of the in-flow turbulence and the differences in airfoil response. This study also assesses the direct link between the surface pressure response of the airfoil and the far-field noise through near-to-field coherence. The paper is organized as follows. Section II provides a detailed explanation of the facility and the experimental setup, including instrumentation and post-processing techniques. The observations and discussions of the paper begin with the far-field noise in Sec. III, followed by the mean flow pressure field analysis in Sec. IV. The spectral analysis of the velocity fluctuation in the turbulent inflow along the stagnation streamline is assessed in Sec. V. The airfoil response to the turbulent flow is presented and discussed in Sec. VI, and its link to the turbulent in-flow is assessed through pressure–velocity coherence study in Sec. VII. The near-to-far coherence analysis is presented in Sec. VIII. Finally, concluding remarks are given in Sec. IX.

II. MEASUREMENT SETUP

The interaction of a turbulent flow and an airfoil is a complex phenomenon, which requires a comprehensive assessment of the flow field around the leading edge and the response of the airfoil. The experiments were conducted in the aeroacoustic wind tunnel facility at the University of Bristol. The aeroacoustic wind tunnel is a temperature-controlled closed-loop, open-jet type with a $500 \times 775\ \text{mm}^2$ rectangular nozzle exit area and is capable of delivering free stream velocities up to 40 m/s. The nozzle opens into an anechoic chamber, which has the dimensions of 6.7 m in length, 4 m in width, and 3.3 m in height, and is acoustically treated with glass wool wedges to achieve a cutoff frequency of $f = 160$ Hz. The turbulence interaction study is performed with a heavily instrumented NACA0012 airfoil with a chord of $c = 200$ mm.

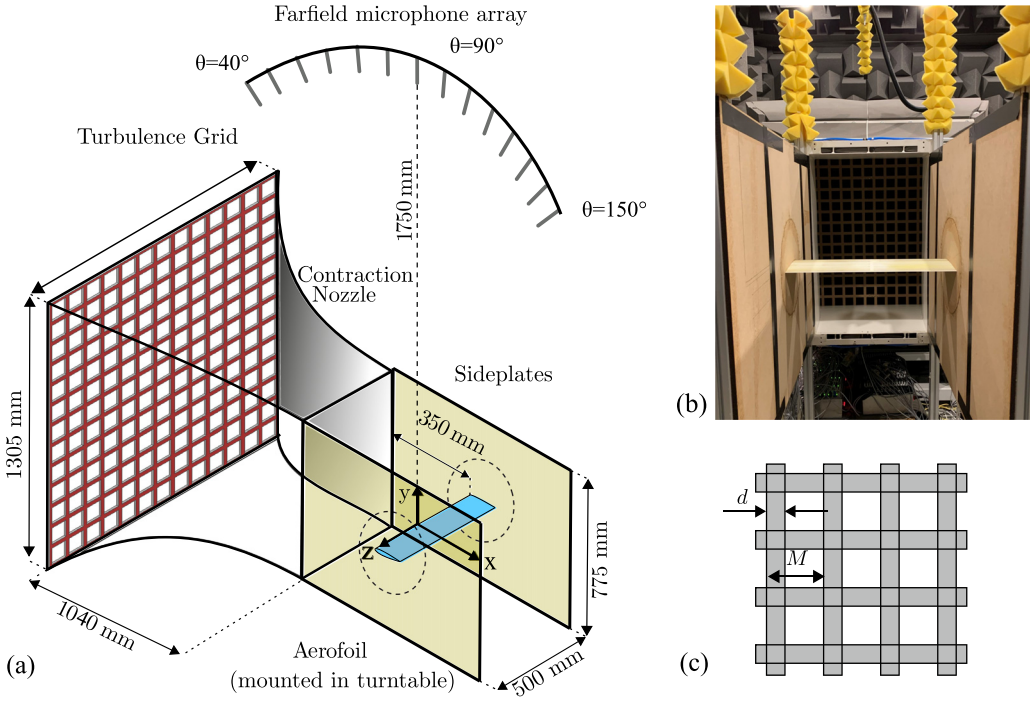

FIG. 1. The experimental setup in the aeroacoustic facility: (a) the schematic of the setup, (b) a picture of the setup, and (c) the turbulence grid geometry definition.

The reference Cartesian coordinate system (x, y, z) is located at the stagnation point on the leading edge of the airfoil to describe the details of the experimental setup. A schematic of the experimental setup is provided in Fig. 1 with the details of the passive grid located inside the nozzle to generate a highly turbulent flow. This section details the experimental setup including, turbulent flow generation, flow characterization using constant temperature anemometry (CTA) hot-wire apparatus, unsteady surface pressure measurements, and far-field noise measurements.

A. Airfoil configuration

A NACA0012 airfoil with a chord of $c = 200$ mm, a span of $s = 500$ mm, and a leading edge radius $r = 3.17$ mm, as depicted in Fig. 2, was used in this study. The airfoil was positioned at the center of the potential core of the wind tunnel (350 mm downstream of the contraction nozzle outlet at $x = 0$ mm) and is mounted within sideplates to ensure a roughly two-dimensional flow. The airfoil was heavily instrumented with steady and unsteady surface pressure measurement transducers. The instrumentation was implemented by means of brass tubes installed into pre-determined channels over the airfoil and smoothed into the surface of the airfoil using two-part epoxy resin. The smooth surface of the airfoil and the epoxy resin was achieved by sanding, incrementally increasing the grit number up to 600 to achieve an approximate surface roughness of $Ra = 0.13 \times 10^{-6}$ m. In order to alleviate high pressure attenuation of the signal, the pressure taps are drilled perpendicular to the airfoil surface using a 0.4 mm drill bit. The 88 unsteady surface pressure measurement

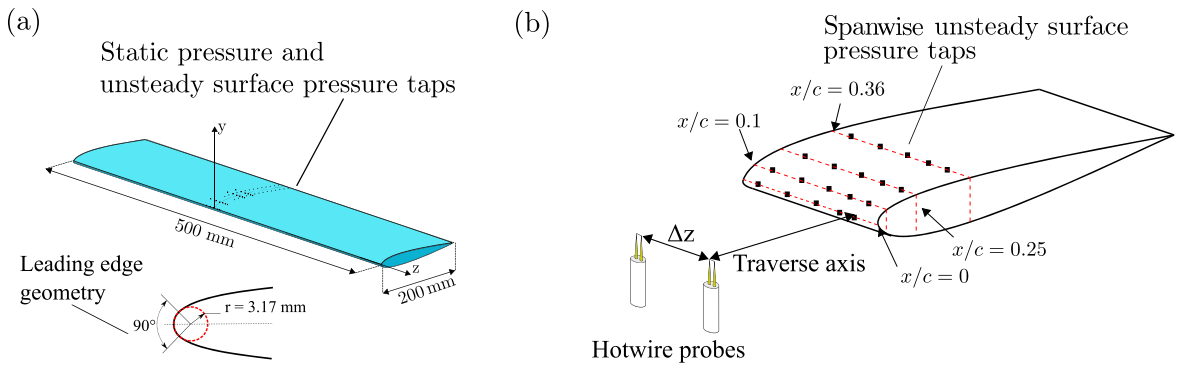

FIG. 2. The schematics of the experimental setup including (a) the airfoil and (b) a closer view of the spanwise measurement locations.

taps were connected to Panasonic WM-61A condenser microphones using a remote sensor configuration. For a more detailed explanation on the unsteady surface pressure measurement technique by remote sensors, see Mayer *et al.*[47] and Sagrado.[48] The remote sensor microphones were calibrated *in situ* for both phase and magnitude referenced to a single GRAS 40PL microphone, which has a flat sensitivity for a broad range, i.e., 10 Hz to 10 kHz. The reference GRAS 40PL microphone was calibrated using a GRAS 42AA pistonphone calibrator. The unsteady surface pressure measurement was acquired at a rate of 2^{15} Hz for 16 s. The unsteady surface pressure measurement locations were distributed over the entire chord of the airfoil for streamwise measurements, i.e., $0 < x/c < 0.92$. Moreover, in order to obtain information along the span of the airfoil, at four streamwise locations, i.e., $x/c = 0$, 0.1, 0.25 and 0.36, measurements at four spanwise separations were acquired, i.e., $\Delta z/r = 1.67$, 3.43, 5.47 and 7.97. The 36 static pressure measurement locations cover the chord of the airfoil between $0 < x/c < 0.92$. Steady pressure data were obtained from two Chell MicroDaq-32 pressure acquisition systems, and sampled for 32 s at a sampling frequency of 1000 Hz. The streamwise locations of the steady and unsteady pressure measurements are provided in Table I.

B. Far-field measurement

Noise generated due to the interaction between the turbulent flow and the airfoil was measured with a far-field microphone array. The array consisted of 23 GRAS 40PL free-field microphones, which are arranged on an arc in 5° increments between polar angles of 40° and 150°. The center of the arc is positioned such that the microphone at polar angle $\theta = 90°$ is directly positioned above the leading edge of the airfoil at a distance of $y = 1.75$ m. Each microphone was calibrated prior to the tests using a GRAS 42AA pistonphone calibrator, reducing microphone uncertainty to ±0.2 dB.

C. Turbulence generation

The normal smooth operation of the aeroacoustic facility has a freestream turbulence intensity of less than 0.2%.[49] To enable a turbulence interaction noise study, the turbulence intensity of the flow is elevated by utilizing passive turbulence grids placed within the contraction nozzle of the wind tunnel, 1040 mm upstream of the nozzle exit. The grid position within the contraction nozzle had a high contraction ratio which does not affect the normal background noise of the wind tunnel jet while delivering a high-level turbulence intensity.[7] This enables the use of direct measurement of the interaction noise and avoids the use of more complicated techniques such as acoustic beamforming arrays. Moreover, direct far-field noise measurements allow for accurate and reliable low-frequency measurement, noise directivity, and coherence analysis between the near-field and the far-field. Turbulence interaction noise generation can vary significantly based on the integral length scale of the turbulence (Λ_x) relative to the body it is interacting with. Two grids were employed to vary the in-flow turbulence characteristics and address the effect of the turbulence length scale on the interaction noise. Grid 1 was designed to generate integral length scales (Λ_x) of the same order as the leading edge radius ($\Lambda_x \approx r$), whereas grid 2 was designed to generate integral length scales larger than the leading edge radius ($\Lambda_x > r$). The depiction of the grids with the definition of geometric properties is demonstrated in Fig. 1. The geometric properties of grids and the properties of the generated flow are outlined in Table II.

TABLE I. Streamwise locations of the remote sensor transducers for unsteady pressure measurement.

Transducer	x/c	Transducer	x/c
p1	0	p10	0.25
p2	0.03	p11	0.31
p3	0.05	p12	0.36
p4	0.06	p13	0.46
p5	0.08	p14	0.52
p6	0.10	p15	0.66
p7	0.16	p16	0.79
p8	0.17	p17	0.87
p9	0.19	p18	0.92

D. Hot-wire anemometry setup

The flow field around the leading edge was characterized by constant temperature anemometry measurements. Two Dantec 55P16 single-wire probes were used in tandem configuration to obtain two-point correlations and were operated using a Dantec Streamline Pro system with a CTA91C10 module. The data were acquired using a National Instruments PXIe-4499 module mounted in a National Instruments PXIe-1026Q chassis. The data were simultaneously sampled from both probes at a rate of approximately 32 kHz for a duration of 8 s. Both the single-wires were calibrated daily using a Dantec 54H10 calibrator. The uncertainty of the velocity measurement was estimated as 2.72% for a free-stream velocity of 20 m/s. The tandem probes were arranged along the z axis at the center of the jet plume core, see Fig. 2(a). The hot-wire probes were traversed using a ThorLabs LTS300 300 mm translation stage with stepper motor along the x axis with a positioning accuracy of ±5 μm. The probes were initially positioned on the leading edge of the airfoil at $x = 0$, $y = 0$, with the left probe positioned directly in front of the stagnation sensor. The probes were then traversed up to $x = -300$ mm upstream to acquire measurements at 35 streamwise locations. Two-point correlations for a broad range of separation distances were obtained with repeated traverse measurements with the separation distance ranging between $5.3 < z < 27$ mm (corresponding to $1.67 < \Delta z/r < 6.40$).

III. FAR-FIELD NOISE

We first consider the results of the far-field noise measurements to show the effect of turbulence properties on the radiated noise

TABLE II. Geometric properties of each grid and the flow properties measured at the contraction nozzle exit at a freestream velocity of $U_\infty = 20$ m/s.

Grid	Diameter d (mm)	Mesh M (mm)	Solidity, σ	Turbulence intensity, TI (%)	Integral length scale, Λ_x (mm)
Grid 1	19	75	0.45	4.8	5.9
Grid 2	45	223	0.35	10.1	10.8

characteristics. Direct noise measurements can highlight the frequency-dependent energy contribution to the overall sound level. In addition, the directivity of the radiated noise can be assessed through the results of the polar array. In the present study, the far-field noise was measured using the polar array described in Sec. II. The far-field results are presented in two forms in Fig. 3. The first is the frequency-energy content of the pressure fluctuations measured by the microphone at $\theta = 90°$, which is directly above the leading edge of the airfoil. The power spectrum, ϕ_{pp} of the pressure fluctuations was estimated using Welch[50] method, where the data from the transducers were segmented for 32 equal lengths with 50% overlap and windowed by the Hamming function, and the resulting spectrum had a frequency resolution of $\Delta f = 2$ Hz. The power spectral density results (PSD) are presented in terms of dB/Hz and calculated as, $10\log_{10}(\phi_{pp}/p_0^2)$, where $p_0 = 20$ μPa is the reference sound pressure. The second form of the far-field noise results presentation is in terms of the overall sound pressure level (OASPL), which is calculated for each microphone over the polar array to display the directivity of the noise radiation. The OASPL is calculated by integrating the energy spectrum over a pre-determined frequency range. The non-weighted OASPL results are calculated for each microphone as $10\log_{10}\int(\phi_{pp}(f)/p_0^2)df$, where the integration of the PSD data is carried out over the frequency range of $f = 160$–$20\,000$ Hz.

Figure 3(a) displays the frequency-energy content of the interaction noise observed at the far-field for two inflow conditions in comparison with the associated grid noise and wind tunnel jet background noise at a freestream velocity of $U_\infty = 20$ m/s. Recall that grid 1 generates a flow with a turbulence intensity of 4.8% and integral length scale of $\Lambda_x = 5.9$ mm, and grid 2 generates a flow with a turbulence intensity of 10.1% and $\Lambda_x = 10.8$ mm. The results are presented for the microphone located at a polar angle of $\theta = 90°$, directly above the leading edge of the airfoil. The energy content of the background noise of the wind tunnel jet and the grid noise are almost identical, signifying that the self-noise of the grids does not affect the airfoil noise. Examining Fig. 3(a), it is apparent that the airfoil generates significantly higher noise when interacting with the flow produced by grid 2 than grid 1. The small broadband hump in the results of the NACA0012 airfoil for the inflow generated by grid 1 is a footprint of grid self-noise.[7] As seen from the results in Fig. 3(a), the turbulence interaction can lead to significant noise increase at low and mid-frequencies.[27] This will also be the frequency range of interest in our near-field analyses provided below, including energy spectrum analysis, airfoil response, and near-field to far-field coherence investigations. A detailed discussion on the noise characteristics of the turbulence grid, and interaction noise can be found in authors recent paper.[7] Figure 3(b) presents the OASPL directivity results for the interaction noise generated for the two different turbulent inflows along with the grid noise and wind tunnel jet background noise at a freestream velocity of $U_\infty = 20$ m/s. The OASPL directivity results are presented for polar angles of $40° < \theta < 135°$, where $\theta = 40°$ is the upstream as presented in Fig. 3(b). The directivity results suggest that the interaction noise generated by the airfoil in both turbulent flows generate significantly higher noise over the background noise level. Moreover, the OASPL results obtained from the flow generated by grid 2 is almost double that of the flow generated by grid 1 over the background level. Finally, there is no apparent change to the directivity patterns for both cases over the majority of angles presented. At the far reaches of the array, (i.e., $\theta < 50°$ and $\theta > 125°$), there is a reduction in the OASPL for the results of the grid 1 case, compared to the results of the grid 2 case. The results underline the effect of the inflow turbulence characteristics on the interaction noise. The increased level of turbulence intensity and integral length scale generated by grid 2 are attributed to the increased turbulence interaction noise.

IV. MEAN FLOW PRESSURE FIELD

In this section, we examine the effect of different inflow conditions on the mean aerodynamic loading using the mean wall-pressure coefficient and the root mean square (r.m.s.) of wall-pressure coefficient results. The results are presented for a freestream velocity of $U_\infty = 20$ m/s, corresponding to a chord-based Reynolds number of $Re = 2.5 \times 10^5$. Mean wall-pressure data for the airfoil are presented as non-dimensional mean pressure coefficient (C_p) and root mean

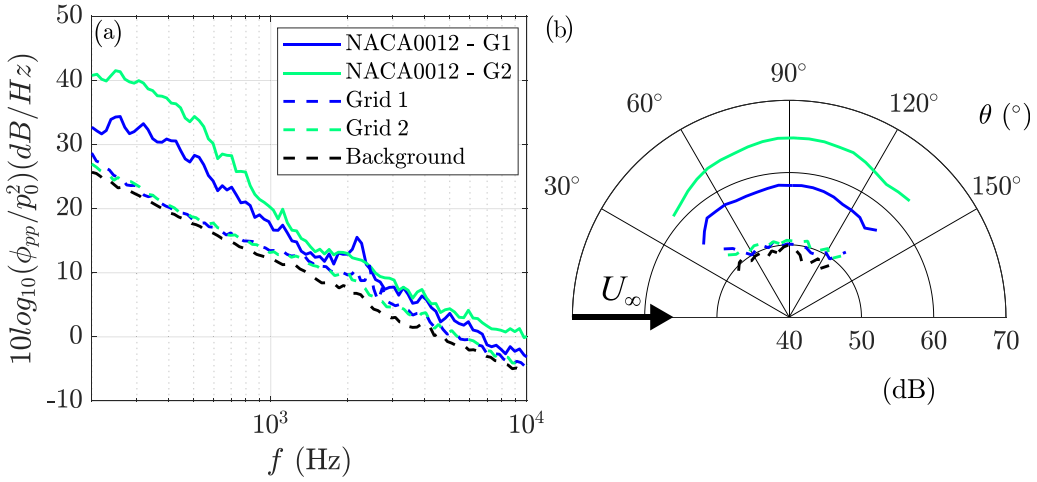

FIG. 3. Far-field noise generated by a NACA0012 airfoil immersed in the turbulent flow generated by two turbulence grids of differing geometric properties compared with the grids' self-noise, and the background noise of the wind tunnel jet for (a) the energy spectra measured at the 90° microphone and (b) overall sound pressure level directivity.

square (r.m.s.) of the pressure coefficient $C_{p,rms}$. The mean wall-pressure coefficient is defined as $C_p = (p - p_\infty)/(p_s - p_\infty)$, where p_∞ is the static pressure of the flow, and p_s is the airfoil stagnation pressure. The root mean square pressure fluctuation is defined as $C_{p,rms} = (p - \bar{p})^{0.5}/(p_s - p_\infty)$, where $\bar{p}$ is the measured mean pressure. The C_p and $C_{p,rms}$ results are presented for the laminar inflow case and the two turbulent inflows generated by grid 1 and grid 2. The laminar flow case is included here as this is previously used to validate the pressure distribution of the airfoil against XFoil predictions.[29,51] Recall that Table II reports the flow properties generated by each grid.

Figure 4 presents the C_p distribution over the airfoil for $\alpha = 0°$. As the airfoil and the pressure field around the airfoil are symmetric, the presented results are average values recorded on the pressure and suction side of the airfoil for each chordwise (streamwise) location. The results reveal that each inflow condition yields in comparable C_p values, signifying that the inflow conditions do not change the mean pressure distribution over the airfoil. However, $C_{p,rms}$ results show a strong dependency to the inflow condition, despite a similar overall behavior along the chord. The highest level of pressure fluctuation over the airfoil is generated by grid 2, which generates a turbulent flow with larger flow structures and higher turbulence intensity. The $C_{p,rms}$ results for the grid 1 case are slightly higher than the laminar inflow case, yet they display a similar behavior over the chord. It is worth noting that an increase in the turbulence intensity level from 0.2% (laminar inflow) to 4.8% (grid 1) does not affect the C_p and $C_{p,rms}$ magnitude significantly over the airfoil. However, the $C_{p,rms}$ results from grid 2 case shows a substantial increase over the region $0 < x/c < 0.5$. The results suggest that an increase in turbulence intensity may not directly affect the C_p and $C_{p,rms}$ distribution, and there may be other governing mechanisms that dictate the change in the $C_{p,rms}$. As the mean pressure field shows little dependency on the turbulence inflow conditions, it would be reasonable to consider that it will not contribute to the significant difference in the far-field noise results between the two cases. The upstream velocity field is explored next to understand how inflow with different conditions evolve (distorts) in the vicinity of the airfoil.

V. TURBULENT IN FLOW AND STAGNATION

The presence of the airfoil in the flow creates a velocity stagnation around the leading edge which is felt far upstream of the airfoil. To elucidate how the stagnation point affects the upstream velocity field, velocity measurements were acquired by hot-wire measurement, utilizing a single-wire probe traversed from directly in front of the leading edge to five leading edge radii upstream, i.e., $-5 < x/r < -0.01$. Figure 5(a) presents the velocity change along the streamwise direction, measured by a single-wire probe for both the turbulent inflows generated by grid 1 and grid 2, normalized by the freestream velocity, $U_\infty = 20$ m/s. Additionally, Fig. 5(b) presents the root mean square of the velocity fluctuations for the same upstream range for both turbulent inflow cases, normalized by the root mean square of the velocity fluctuations of the freestream flow (u'_0) for each respective grid at $x/r \approx -32$. It is worth noting that this manuscript adopts the notation used by Hinze[52] for velocity fluctuations (u) and root mean square velocity fluctuations (u'). Evident in Fig. 5, both flows generated by grid 1 and grid 2 experience a comparable effect due to the stagnation between $-5 < x/r < -1.5$. However, between $-1.5 < x/r < -0.01$, the velocity magnitude differs substantially between the two cases where the flow generated by grid 2 experiences a more significant reduction in velocity. The r.m.s. velocity fluctuation results presented in Fig. 5(b) reveal a drastic variation due to stagnation. The magnitude of the r.m.s. velocity fluctuation reduces to a trough approaching the leading edge at around $x/r = -0.15$. The r.m.s. magnitudes then experience a significant increase in the proximity of the leading edge, which is consistent with the previous experimental observations.[34] Consistent with the results of mean velocity, the results of velocity fluctuations produced by grid 2 appear to be more sensitive to the presence of the airfoil and have a more significant reduction when compared with the results from grid 1 case. Furthermore, in the vicinity of the leading edge, the velocity fluctuation values of the flow

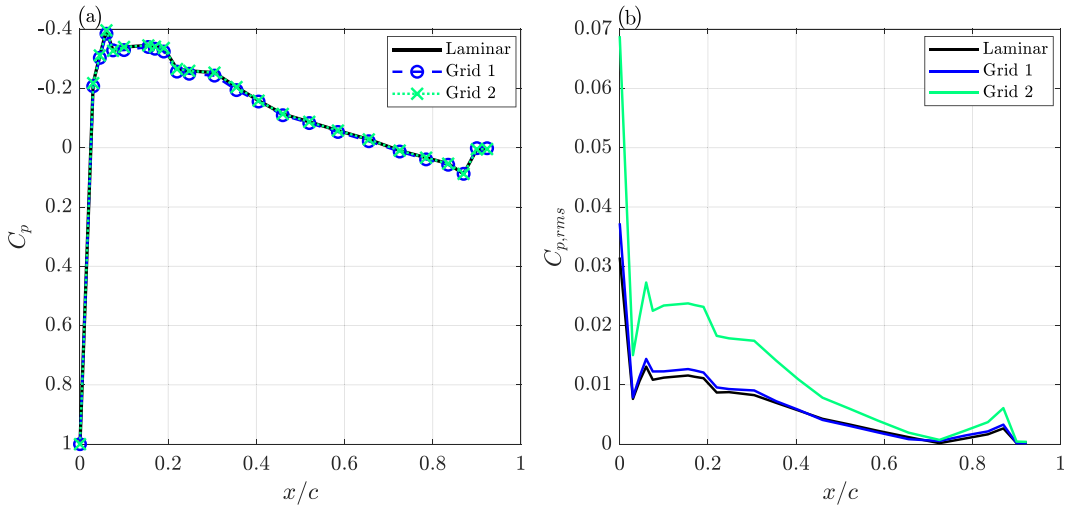

FIG. 4. Comparison of (a) non-dimensional mean pressure coefficient and (b) (C_p) and root mean square of the mean pressure coefficient ($C_{p,rms}$) for the NACA 0012 airfoil in a smooth and two turbulent flows generated by grid 1 and grid 2.

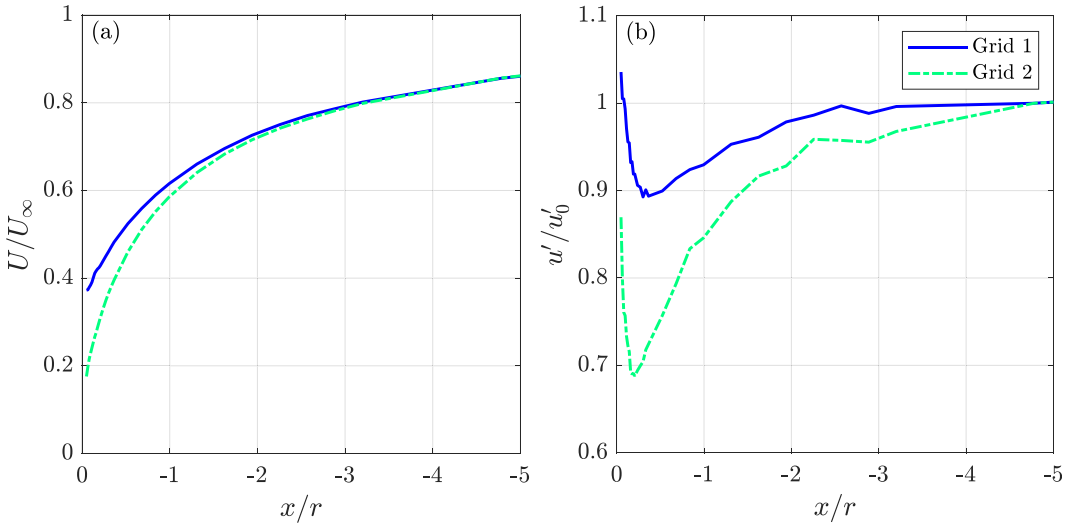

FIG. 5. Stagnation line flow properties measured by single-wire probe for (a) normalized flow velocity (U/U_∞) and (b) normalized r.m.s. velocity fluctuation (u'/u'_0) at a free-stream velocity of $U_\infty = 20$ m/s.

generated by grid 1 exceed the fluctuation of the upstream value, $u'/u'_0 = 1.04$. In contrast, the r.m.s. velocity fluctuation of the flow generated by grid 2 does not increase beyond $u'/u'_0 = 0.88$. As suggested by Amiet,[18] the re-distribution of the energy into the upwash component is linked to the noise generation. Although the r.m.s. velocity fluctuation from grid 2 displays a more significant reduction compared to that of grid 1, it is worth noting that the recovery of the r.m.s. of velocity fluctuation for the grid 2 case is also more significant.

To understand the frequency-energy content of the velocity fluctuations along the stagnation line for the inflow generated by each grid (the line which passes through $y = 0$ and $z = 0$ and extends through $\pm x$ axis), the power spectrum of the velocity fluctuations (ϕ_{uu}) was estimated using Welch[50] method. The power spectral density results (PSD) of the velocity fluctuations are presented in terms of dB/Hz and calculated as, $10\log_{10}(\phi_{uu}/u'^2_0)$, where u'_0 is the r.m.s. velocity fluctuation of the freestream measured at $x/r \approx -32$. Figure 6 presents the velocity fluctuation PSD for the flow generated by grid 1 and grid 2. The results are presented for six locations along the stagnation line between $-4.74 < x/r < -0.01$ and the freestream value, for both the flow generated by grid 1 [Fig. 6(a)] and grid 2 [Fig. 6(b)]. The PSD results in Fig. 6 clearly demonstrate a significant change in the high-frequency energy content between cases, potentially signifying different decay behaviors. Evident in Fig. 6, the flow from grid 1 is subject to two high-frequency decay gradients where all the velocity PSD

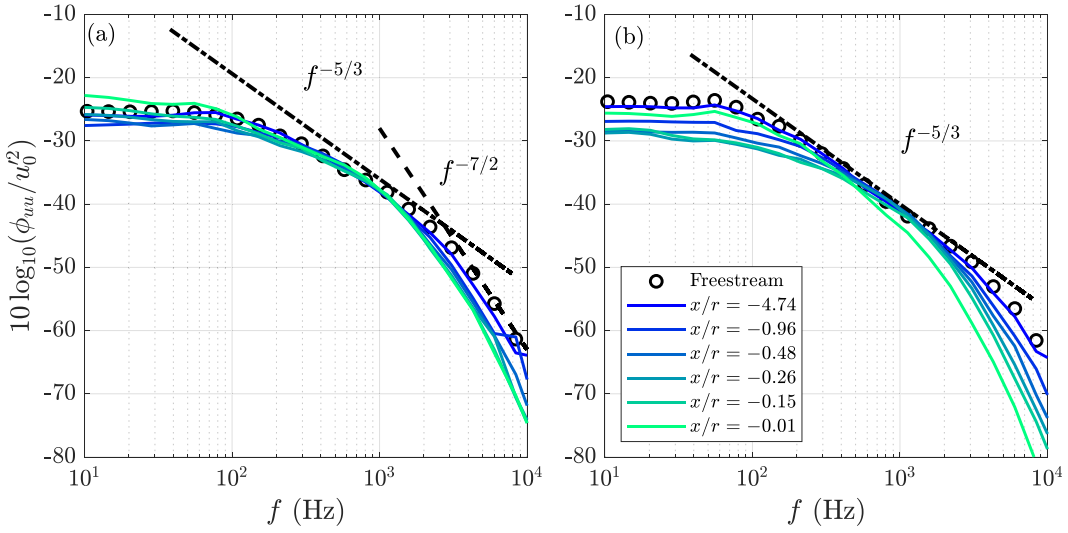

FIG. 6. Power spectral density of the velocity fluctuation along the stagnation line, upstream of the NACA 0012 airfoil leading edge between $-4.74 < x/r < -0.01$ measured by a single-wire probe for two turbulent inflows produced by (a) grid 1 and (b) grid 2 at a freestream velocity of $U_\infty = 20$ m/s.

profiles collapse, i.e., $f^{-5/3}$ and $f^{-7/2}$. However, the results of the grid 2 case exhibit only one decay gradient where all the PSD profiles collapse, i.e., $f^{-5/3}$ at mid-frequencies. Furthermore, the velocity PSD decay gradient increases toward the leading edge at higher frequencies. The velocity fluctuation PSD results of the flow generated by grid 2 show a reduction in the energy content across the full spectra as it approaches the leading edge of the airfoil for the region $-4.74 < x/r < -0.25$. This result coincides with the reduction of r.m.s. velocity fluctuations for the same region in Fig. 5(b). Close to the leading edge $-0.25 < x/r < -0.01$, a noticeable increase in the energy content at low-frequency is evident. In contrast, the energy spectra of the flow generated by grid 1 have a twofold behavior, which is not concurrent across the full frequency range. At higher frequencies, $f > 1000$ Hz, there is a reduction in the magnitude of the velocity fluctuation PSD approaching the leading edge. At lower frequencies, $f < 100$ Hz, there is a small reduction in low-frequency energy content approaching one leading edge radius from the airfoil, $x/r > -1$. Inside one leading edge radius from the airfoil, $x/r < -1$, the low-frequency energy content increases significantly. However, this result does not mimic the r.m.s. velocity fluctuation results observed in Fig. 5. The trough in the r.m.s. velocity fluctuation ($x/r \approx 0.5$) is closer to the leading edge than the location of minimum velocity fluctuation PSD level ($x/r \approx 1$) in Fig. 6(a). Another interesting observation is the appearance of a crossover frequency for each case, a frequency where there is no significant change in any distance from the leading edge stagnation point. The crossover frequency for the results of grid 1 case is observed at approximately $f \approx 1000$ Hz, whereas for grid 2 case is at approximately $f \approx 500$ Hz. For both sets of the results, this corresponds to the region where the decay gradient is $f^{-5/3}$.

To further understand the frequency-dependent contributions to the velocity fluctuations, the pre-multiplied energy spectra, i.e., $f\phi_{uu}/u_0^2$, are presented. To ease the interpretation of the results, both energy spectra were normalized by the square of the freestream level of velocity fluctuation, u_0^2. Presenting the PSD of the velocity fluctuations multiplied with the frequency further accentuates the high-frequency behavior, where decay gradients are evident along the stagnation stream. Furthermore, the presentation of the energy spectra in Fig. 7 enables comparison of energy contribution, where the equal area under the curve represents an equal contribution to energy.[53] In other words, the pre-multiplied energy spectra profiles that retain a quasi-plateau shape represents a relatively even distribution of the energy across different scales. The velocity fluctuation pre-multiplied energy slightly reduces over a broad range of frequencies, except a narrowband region at around $f = 1000$ Hz, compared to the freestream results at $x/r \approx 32$ in the case of grid 1. However, at the vicinity of the airfoil ($x/r = -0.01$), the low-frequency energy content exceeds the corresponding freestream level. Considering the r.m.s. velocity fluctuation results discussed in Fig. 5(b) together with the pre-multiplied energy spectra results, it is reasonable to conclude the following points. The reduction in the r.m.s. velocity fluctuations is mainly driven by the decrease in low-frequency energy content. Moreover, the overshoot of the r.m.s. velocity fluctuation, i.e., the recovery beyond the freestream level, is mainly driven by the energy content increase at $f < 100$ Hz, where the pre-multiplied energy levels surpass the freestream levels. Comparing the two cases under examination, the energy content for the grid 2 case is slightly higher than the grid 1 case at the far upstream, where the effect of the airfoil is not felt. Nevertheless, a drastic reduction of the energy content is evident as the flow approaches the leading edge until the vicinity of the stagnation point, $x/r = -0.01$, where a substantial increase in low-frequency energy is accompanied by a drastic reduction at high-frequency energy content. Similar to the discussions for the grid 1 case, considering the r.m.s. velocity fluctuation results together with the pre-multiplied energy spectra, we can conclude that the reduction in the low-to-mid frequency drives the decreased level of the r.m.s. velocity fluctuation. Furthermore, the recovery of the r.m.s. velocity fluctuation to the upstream levels is driven primarily by the increased low-frequency energy content.

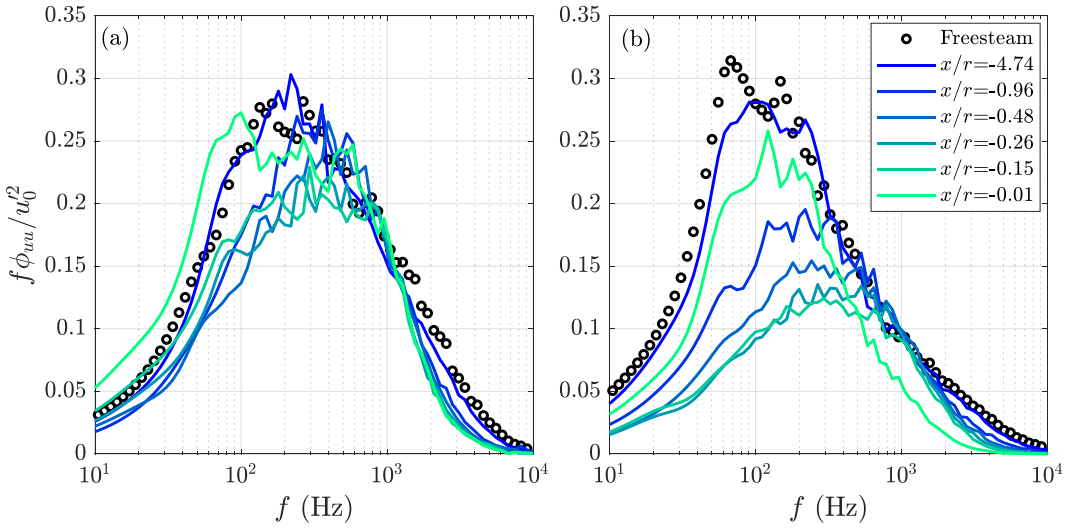

FIG. 7. Pre-multiplied energy spectra of the velocity fluctuations $f\phi_{uu}/u_0{}^2$ along the stagnation line, measured upstream of the NACA 0012 airfoil leading edge between $-4.74 < x/r < -0.01$ by tandem single-wire probes for two turbulent inflows produced by (a) grid 1 and (b) grid 2 at a freestream velocity of $U_\infty = 20$ m/s.

The nature of the velocity fluctuations can be realized by examining the probability density function (PDF) of the velocity fluctuations, which allows an in-depth understanding of the occurrence, strength and symmetry of the fluctuations along the stagnation line. Figure 8 presents the PDF of the velocity fluctuations for the flow generated by grid 1 and grid 2 at six locations along the stagnation line between $-4.74 < x/r < -0.01$ in comparison with the results obtained at $x/r \approx 32$, which represents the undisturbed flow at an upstream location. The PDF results for grid 1 case show no significant change compared to the freestream PDF. Along the stagnation line, approaching the minimum fluctuation location (i.e., $x/r \approx -0.4$, see Fig. 5), there is a slight reduction in the tails of the distribution. Nevertheless, this recovers in the region where distortion is evident (i.e., $x/r = -0.01$). On the contrary to the results for the grid 1 case, the PDF results for the grid 2 case, shown in Fig. 8(b), exhibits a change in the nature of PDF results, i.e., a pronounced deviation from the freestream results, which signifies an increase in the level of velocity fluctuations. Approaching the point of minimum velocity fluctuations (i.e., $x/r \approx -0.25$, see Fig. 5), there is a significant reduction in the width of the PDFs, signifying a reduction in the magnitude of the velocity fluctuations. In the region of turbulence distortion, $-0.24 < x/r < -0.01$, there is a recovery in the positive tail of the PDF, yet a further reduction in the negative tail of the PDF. This is exacerbated close to the leading edge $x/r = -0.01$, where the peak in the PDF is no longer centered at $u = 0$ and is approximately centered at $u \approx -0.75$, with a significantly deviated tail in the positive direction. The behavior signifies an increase in the velocity fluctuations in one direction and is no longer uniform about $u = 0$.

The changes in the velocity fluctuation PDFs are elaborated with the skewness' and kurtosis analysis along the stagnation line. Skewness, $S(u)$, is the third moment of velocity fluctuation u and provides insight into the shape of the PDF of u, and is defined as $S(u) = \overline{u^3}/(\overline{u^2})^{3/2}$. It is worth noting that a symmetric distribution of the velocity fluctuation PDF denotes a skewness value of zero.[54] Kurtosis (or flatness) is the fourth moment of u and is defined as $K(u) = \overline{u^4}/(\overline{u^2})^2$. The theoretically expected kurtosis value for a freely decaying turbulence is $K(u) = 3$, which indicates that the PDF of the velocity fluctuations has a Gaussian distribution.[54] Intermittent, large deviations from u indicate a high kurtosis, where a time series with deviations close to the mean is expected to have a low kurtosis value. Figure 9 presents the skewness (left) and kurtosis (right) of the velocity fluctuations along the stagnation line for both the flows generated by grid 1 and grid 2 for a freestream velocity of $U_\infty = 20$ m/s. At a first glance, a noticeable difference between the skewness and kurtosis results of grid 1 and grid 2 cases is evident, which is consistent with the previous discussions on Fig. 8. For the upstream region of the airfoil leading edge ($-5 < x/r < -1$), the results of both flows exhibit the skewness and kurtosis characteristics of a freely decaying turbulent flow, with expected values of $S(u) \approx 0$ and $K(u) \approx 3$. However, a substantial increase in both the skewness and kurtosis values are evident in the vicinity of the leading edge of the airfoil for the flow generated by grid 2. In addition, skewness and kurtosis values display a minute change compared to the upstream results for the grid 1 case. These results suggest large, positive velocity fluctuations in the vicinity of the airfoil leading edge for the flow generated by grid 2. Furthermore, the results hint at a change in the nature of the turbulence interaction with a change in the turbulence characteristics, i.e., turbulence intensity and integral length scale of the coherent structures.

The temporal characteristics of the flow approaching to the airfoil leading edge can be assessed from the autocorrelation of the velocity fluctuations, which is defined as $R_{uu}(\tau) = \overline{(u(t+\tau)u(t))}/u'^2$, where u is the velocity fluctuation measured by the single-wire probe at streamwise location x/r, u' is the root mean square of the velocity fluctuation, and τ is the time-delay. Figure 10 presents the results of the velocity autocorrelation for both flows generated by grid 1 and grid 2, measured along the stagnation line for a freestream velocity of $U_\infty = 20$ m/s. The time delay is non-dimensionalized by the local velocity at the corresponding measurement location, U_x, and the leading edge radius, r. Figure 10 further highlights the distinctions of the turbulent inflows of each grid, and how they differ in the proximity of

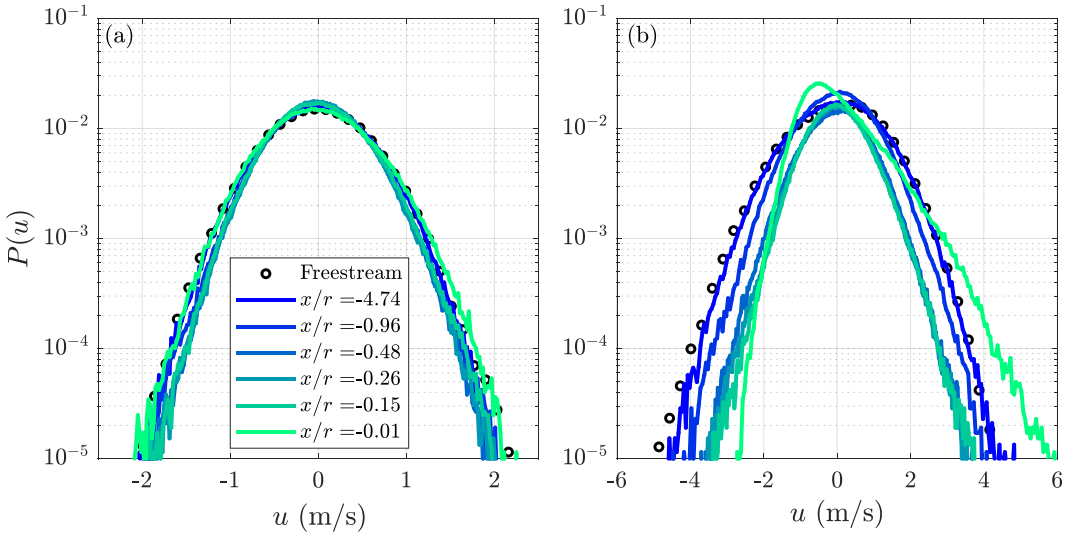

FIG. 8. Probability density function of the velocity fluctuations $P(u)$ along the stagnation line for (a) grid 1 and (b) grid 2 at a freestream velocity of $U_\infty = 20$ m/s.

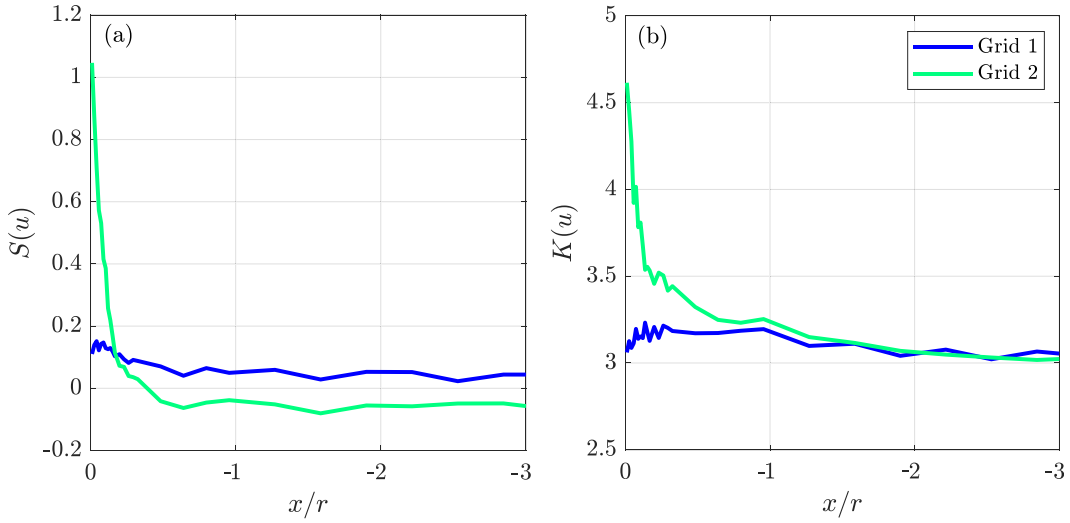

FIG. 9. Skewness [$S(u)$] and Kurtosis [$K(u)$] of the velocity fluctuation along the stagnation line for both inflows generated by (a) grid 1 and (b) grid 2 at a freestream velocity of $U_\infty = 20$ m/s.

the leading edge. Along the stagnation line, the velocity autocorrelation width reduces until $x/r = -0.96$ approaching the leading edge for the grid 1 case. Beyond $x/r = -0.96$, the velocity autocorrelation width increases until the airfoil stagnation point, i.e., $x/r = -0.01$. The increase in the width of the velocity autocorrelation along the stagnation line in the vicinity of the stagnation point appears to be due to large-scale structures, as the initial decay region, which is an indicator of the contribution from the smallest coherent structures in the flow,[55] has no discernible change among cases. The velocity autocorrelation results for the grid 2 case displays a more gradual change compared to the results of the grid 1 case. The results show a significant reduction in the width of the velocity autocorrelation up to $x/r = -0.33$. Beyond this point, as the flow approaches to the stagnation point, the magnitude velocity autocorrelation width reduction decreases. A closer examination of Fig. 10(b) reveals that the initial decay rate of the velocity autocorrelation remains similar within $x/r > -0.33$, which indicates a change in the larger scale structures within the flow field. The further reduction in the velocity autocorrelation width in the results of grid 2 is not observed in grid 1 results. As with Figs. 5–7, the change in the energy content of the flow approaching the stagnation point appears to occur at a different location for each case, alluding to a dependency on the turbulence properties of the inflow.

Having identified the change in the energy content using velocity PSD and the flow behavior using statistical analysis and velocity autocorrelation, we can now study how the flow structures change

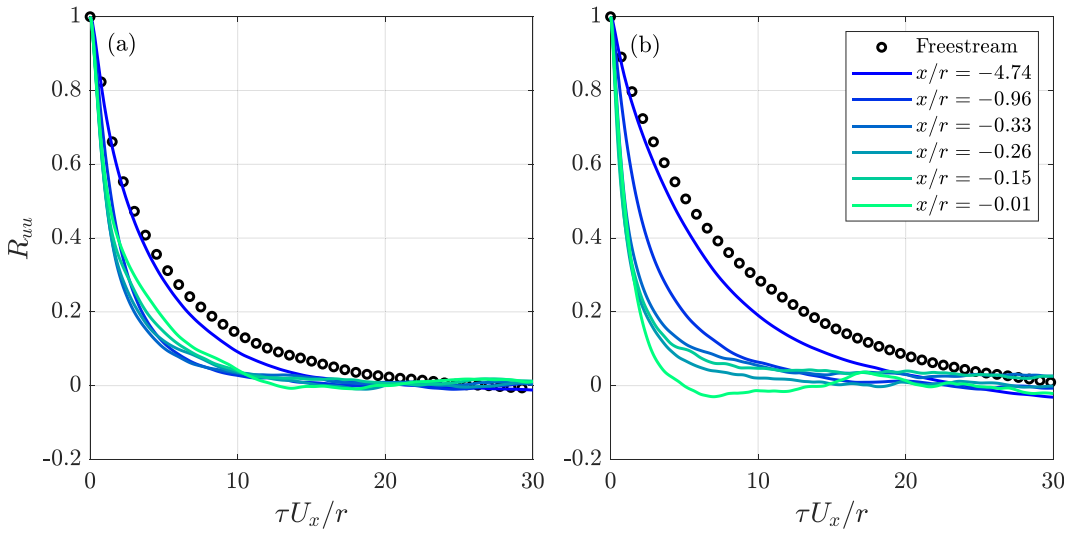

FIG. 10. Velocity fluctuation autocorrelation along the stagnation line for both inflows generated by (a) grid 1 and (b) grid 2 at a freestream velocity of $U_\infty = 20$ m/s.

approaching to leading edge by the spanwise coherence of the velocity fluctuations. Moreover, as the spanwise characteristics of the turbulent structures is an input to the airfoil turbulence noise prediction,[18] it may allow us to bridge the gap between the far-field results and velocity field. The magnitude-squared of the spanwise coherence is calculated as

$$\gamma^2_{u_iu_j}(f,\Delta z) = \frac{|\phi_{u_iu_j}(f)^2|}{|\phi_{u_iu_i}(f)||\phi_{u_ju_j}(f)|}, \tag{1}$$

where $\gamma^2_{u_iu_j}(f,\Delta z)$ is the spanwise coherence calculated between two single-wire probes in a tandem configuration located at z_i and z_j, separated by Δz, and $\phi_{u_iu_j}$ denotes the cross-power spectral density of the velocity fluctuations. Figure 11 shows the spanwise coherence results at six positions along the stagnation line for the flow generated by grid 1 at a freestream velocity of $U_\infty = 20$ m/s. The corresponding r.m.s. velocity fluctuation plots, presented in Fig. 5, is also placed in the plots with a marker showing the measurement location. Figure 11(a) shows the results of the spanwise velocity coherence for the freestream flow measured at $x/r \approx 32$. At this location, the spanwise velocity coherence is observed over the frequency range of $60 < f < 400$ Hz with a peak value of $\gamma^2_{u_iu_j} \approx 0.55$ at the closest spanwise separation, $z/r = 1.67$. As the spanwise separation distance between the probes increases, the level of velocity coherence reduces monotonically. An inspection of the coherence level behavior along the stagnation line reveals that as the flow approaches the stagnation point, the spanwise velocity coherence reduces significantly and reaches to an almost zero level at the leading edge. Recalling the velocity autocorrelation results, which indicates the streamwise timescale of the structures [Fig. 10(a)], at the point where the velocity autocorrelation timescale reaches its fastest decay ($x/r = -0.96$), the spanwise velocity coherence level has more than halved from its upstream value [see Fig. 11(c)]. It is worth mentioning that the streamwise position where the spanwise velocity coherence is observed to be near-zero ($x/r = -0.33$) for all separation distances coincides with the location where the velocity autocorrelation width starts to increase [Fig. 10(a)] and the energy content at low-frequencies increase [Figs. 6(a) and 7(a)].

Figure 12 presents the results of the spanwise coherence of the velocity fluctuations for the flow generated by grid 2 along the stagnation line. At first glance, the results displayed in Fig. 12 show a higher level of spanwise velocity coherence compared to that of grid 1 case. At the freestream location ($x/r \approx 32$), Fig. 12(a), the highest level of velocity coherence is for the freestream location, similar to the grid 1 case. Considering the figure as a whole, the spanwise velocity coherence level reduces for the shorter separation distances up to $x/r = -0.33$, then increases up to the stagnation point. Interestingly, from the upstream of the leading edge ($x/r = -0.96$) to the stagnation point, the level of spanwise velocity coherence for the largest three separation distances ($z/r = 6.40, 4.16$ and 0.96) systematically increases. The comparable level of spanwise velocity coherence for all

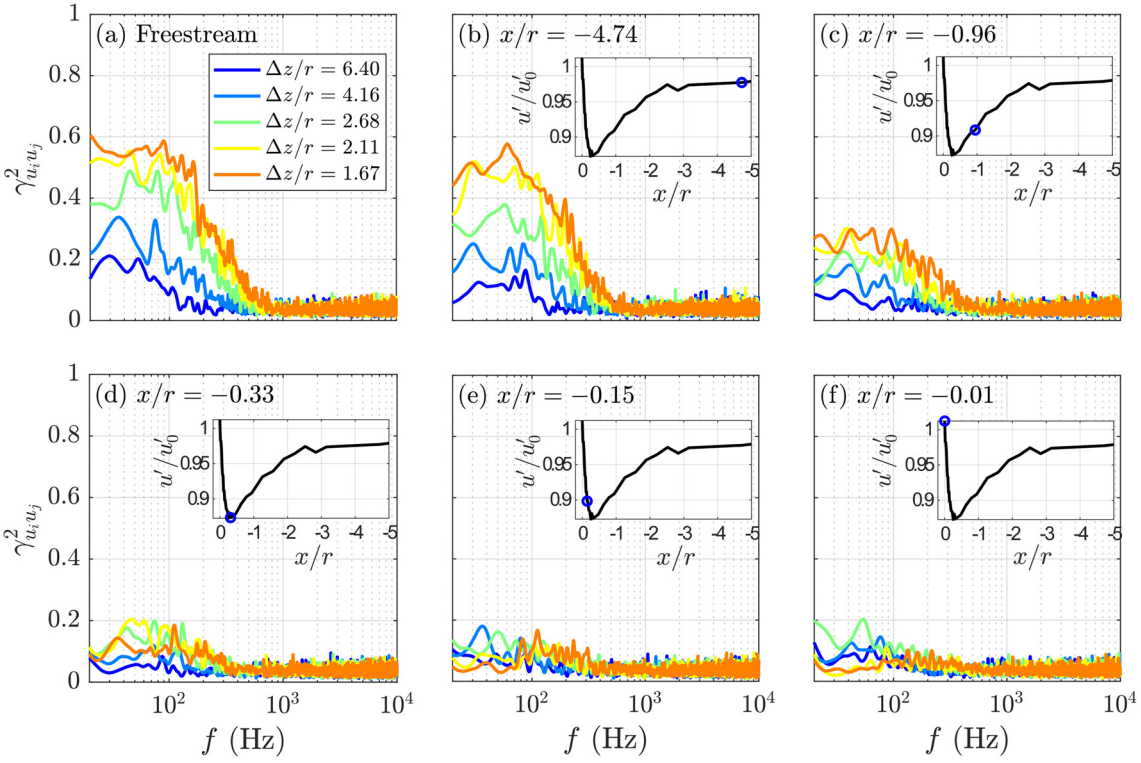

FIG. 11. Spanwise magnitude-square coherence ($\gamma^2_{u_iu_j}$) of velocity fluctuations measured by tandem hot-wire probes at multiple spanwise separations ($\Delta z/r$) for the flow generated by grid 1 for (a) the freestream at $x/r \approx -32$, and locations along the stagnation line (b) $x/r = -4.74$, (c) $x/r = -0.96$, (d) $x/r = -0.33$, (e) $x/r = -0.15$, and (f) $x/r = -0.01$.

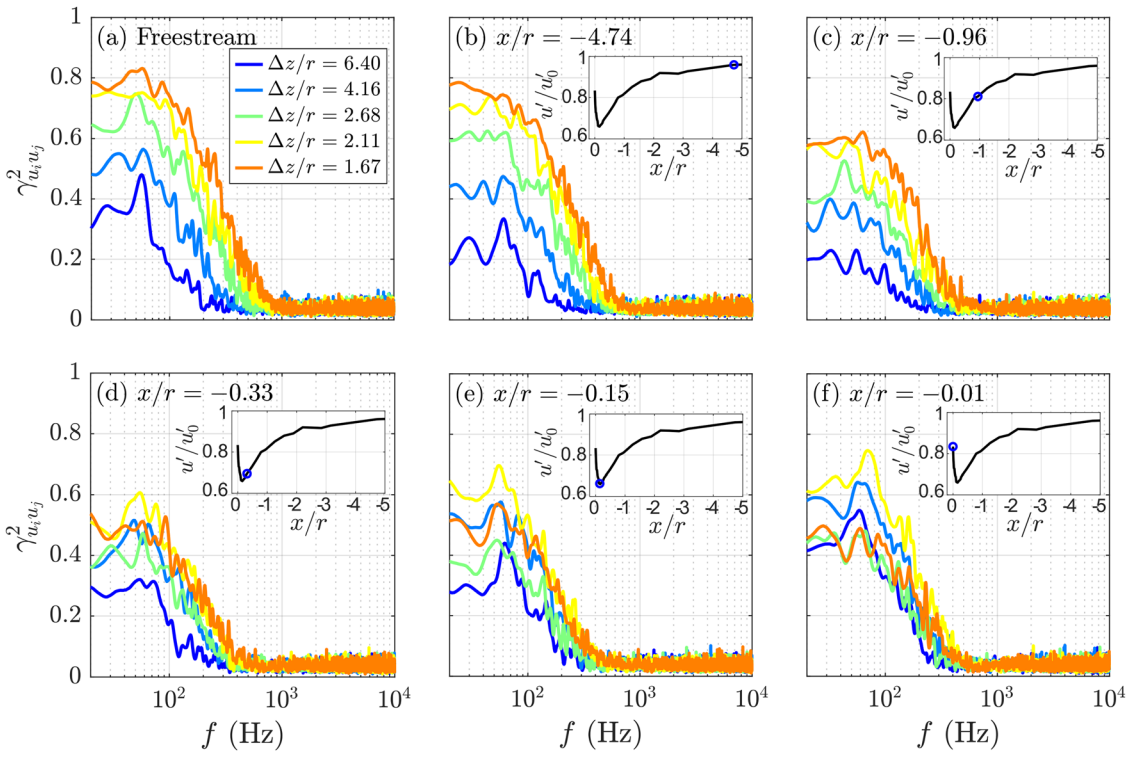

FIG. 12. Spanwise magnitude-square coherence ($\gamma^2_{u_i u_j}$) of velocity fluctuations measured by tandem hot-wire probes at multiple spanwise separations ($\Delta z/r$) for the flow generated by grid 2 for (a) the freestream at $x/r \approx -32$, and locations along the stagnation line (b) $x/r = -4.74$, (c) $x/r = -0.96$, (d) $x/r = -0.33$, (e) $x/r = -0.15$, and (f) $x/r = -0.01$.

separation distances is observed in the vicinity of the stagnation point ($x/r > -0.33$), which suggests that the flow becomes 2D at this point. Moreover, in this region where the flow is considered to become two-dimensional ($x/r > -0.33$), the velocity autocorrelation initial decay rate is consistent as seen in Fig. 10(b). The considerably different behavior of the spanwise velocity coherence between the two cases can be corroborated by the skewness and kurtosis results (Fig. 9), where a significant increase in skewness and kurtosis were observed for the flow generated by grid 2 but not for case grid 1. The results suggest that the increase in the energy content in grid 1 case could be due to the dispersal of the turbulent structures, whereas for the results of grid 2, is due to the distortion of the flow structures in to more two-dimensional structures. The significant difference in the evolution of the flow structures along the stagnation line observed between the two cases may influence the far-field noise observed. The airfoil response to these flows should shed more light on the nuances between the flows.

VI. AIRFOIL RESPONSE

In Sec. V, the upstream effect of the airfoil was characterized for two different flow conditions along the stagnation line. This section focuses on exploring the effect of inflow conditions on the unsteady surface pressure fluctuations over the airfoil in detail.

Analysis of the airfoil response to the turbulent inflows has revealed a significant effect that depends on the turbulence length scale, Λ_x and the turbulence intensity level. Empirical models, such as Amiet's model,[18] suggest that the turbulent inflow dictates the level of the airfoil noise. Figure 13 shows the results of the power spectral density of the surface pressure fluctuations obtained from the pressure transducers along the chord of the NACA0012 airfoil. The figure presents the results for the flow generated by grid 1 on the top row [Figs. 13(a)–13(c)] and grid 2 on the bottom row [Figs. 13(d)–13(f)] for frequencies between $100 < f < 5000$ Hz. To aid the interpretation of the results, Fig. 13 presents the surface pressure PSD results for three sections of the airfoil chord where figure couples [Figs. 13(a) and 13(d), 13(b) and 13(e), and 13(c) and 13(f)] display the results from sensors p1–p7, p8–p12, and p13–p18, respectively. Moreover, each transducer is color coded on the airfoil schematics, and the associated energy spectra result is presented with the same color. Initial inspection of Fig. 13 reveals that for both inflow cases, the highest energy level is generated at the stagnation point (p1), and it exhibits a significantly different spectral distribution with multiple decay gradients compared to the results obtained from the rest of the transducers. Further to this, the frequency energy content of the flow over the entire airfoil, i.e., across all transducers, is significantly higher for the grid 2 case compared to that of grid 1 case. The surface pressure PSD results scale with f^{-7} at high frequencies in the case of grid 1 [Fig. 13(a)], whereas for the results of grid 2 case, PSD results scale with $f^{-7/2}$ [Fig. 13(d)]. After the stagnation point, the surface pressure PSD results over the airfoil leading edge scales with $f^{-5/2}$ [Figs. 13(a) and 13(d)] and reduces steadily with downstream distance, i.e., $0.03 < x/c < 0.19$. As the flow develops along the surface of the

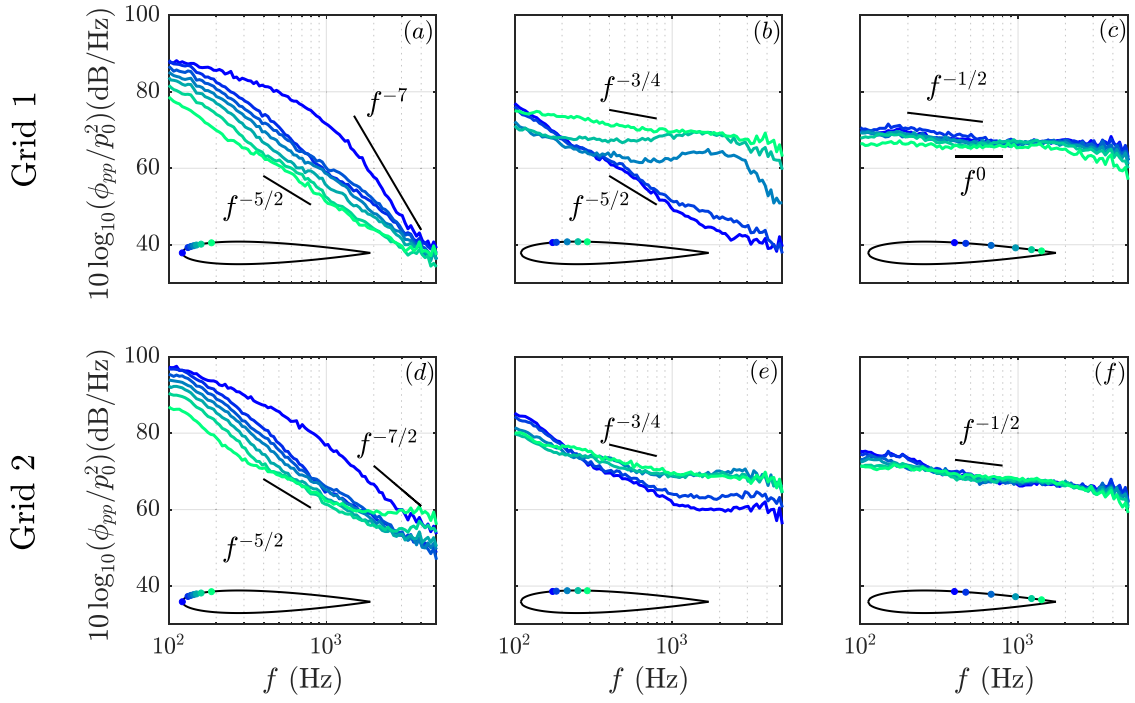

FIG. 13. Power spectral density level of the surface pressure fluctuations over the NACA 0012 airfoil measured by remote sensors: [(a) and (d)] transducers p1–p7 ($0 < x/c < 0.16$), [(b) and (e)] transducers p8–p12 ($0.17 < x/c < 0.35$), and [(c) and (f)] transducers p13–p18 ($0.46 < x/c < 0.92$), for two turbulent inflows produced by grid 1 (top) and grid 2 (bottom).

airfoil, $0.17 < x/c < 0.35$, as shown in Figs. 13(b) and 13(e), the low-frequency energy content of the surface pressure PSD results decrease and the high-frequency energy content increase for both cases. However, the surface pressure energy spectra results clearly demonstrate the distinction between airfoil response in two different turbulent flows as there is a significant shift to the location where the decay rate of the energy spectra changes from $f^{-5/2}$ to $f^{-3/4}$. The energy spectra start to scale with $f^{-3/4}$ later, at around $x/c = 0.25$, for lower *TI* and smaller incoming turbulent structure size, i.e., grid 1 case, compared to the results of the grid 2 case, where the scaling changes at around $x/c = 0.16$. Between $0.46 < x/c < 0.92$, nuances between the surface pressure response of the two flows are evident, as displayed in Figs. 13(c) and 13(f). The surface pressure PSD exhibits a monotonic reduction for the grid 1 case with a change in energy decay rate along the chord line toward the trailing edge. In addition, around $f \approx 1000$ Hz, the energy spectra reaches a plateau with no decay for most of the transducers. On the contrary, surface pressure PSD results for grid 2 case exhibit relatively consistent magnitudes over $0.55 < x/c < 0.92$ and scales with $f^{-1/2}$. Considering the far-field noise prediction models,[18] the results suggest that the leading edge region of the airfoil is mainly responsible for the airfoil–turbulence interaction noise, as the pronounced differences regarding energy levels between grid 1 and grid 2 are observed at around $0 < x/c < 0.2$. However, variations in the surface pressure PSD results between the two turbulent inflows are evident along the entire chord of the airfoil. The increased energy level and earlier change in the spectral distribution of the energy content (PSD) for grid 2 case could be attributed to the elevated far-field noise observed for this case.

Having previously considered the spanwise coherence of the velocity fluctuations approaching the stagnation point, the coherence between the surface pressure fluctuations is considered to understand the spanwise extent of the turbulent structures over the airfoil surface due to its importance in empirical models.[18] The magnitude-squared coherence between the signals obtained from surface pressure measurement locations for various spanwise separation distances (Δz) at multiple streamwise locations (x/r) was calculated as follows:

$$\gamma^2_{p_i p_j}(f, \Delta z) = \frac{|\phi_{p_i p_j}(f)^2|}{|\phi_{p_i p_i}(f)||\phi_{p_j p_j}(f)|}, \tag{2}$$

where $\gamma^2_{p_i p_j}(f, \Delta z)$ is the spanwise coherence calculated between two transducers at the same chordwise position z_i and z_j, separated by Δz, and $\phi_{p_i p_j}$ denotes the cross-power spectral density of the pressure fluctuations. Figure 14 presents the surface pressure fluctuation magnitude-squared coherence for four spanwise separation distances at four streamwise locations, $x/c = 0$, 0.1, 0.25 and $x/c = 0.36$ for the flows generated by grid 1 and grid 2. Schematics displaying the transducer locations are presented to ease the interpretation of the results. At first glance, the elevated coherence magnitudes for the grid 2 case compared to that of case 1 indicates that the spanwise pressure coherence ($\gamma^2_{p_i p_j}$) at the stagnation point is sensitive to the characteristics of the turbulent inflow, as shown in Figs. 14(a) and 14(e). As the flow develops over the leading edge, Figs. 14(b) and 14(f), a strong spanwise pressure coherence is observed for both cases. The similar coherence magnitudes across cases for corresponding transducer pairs suggest a lack of dependency on the turbulent inflow characteristics.

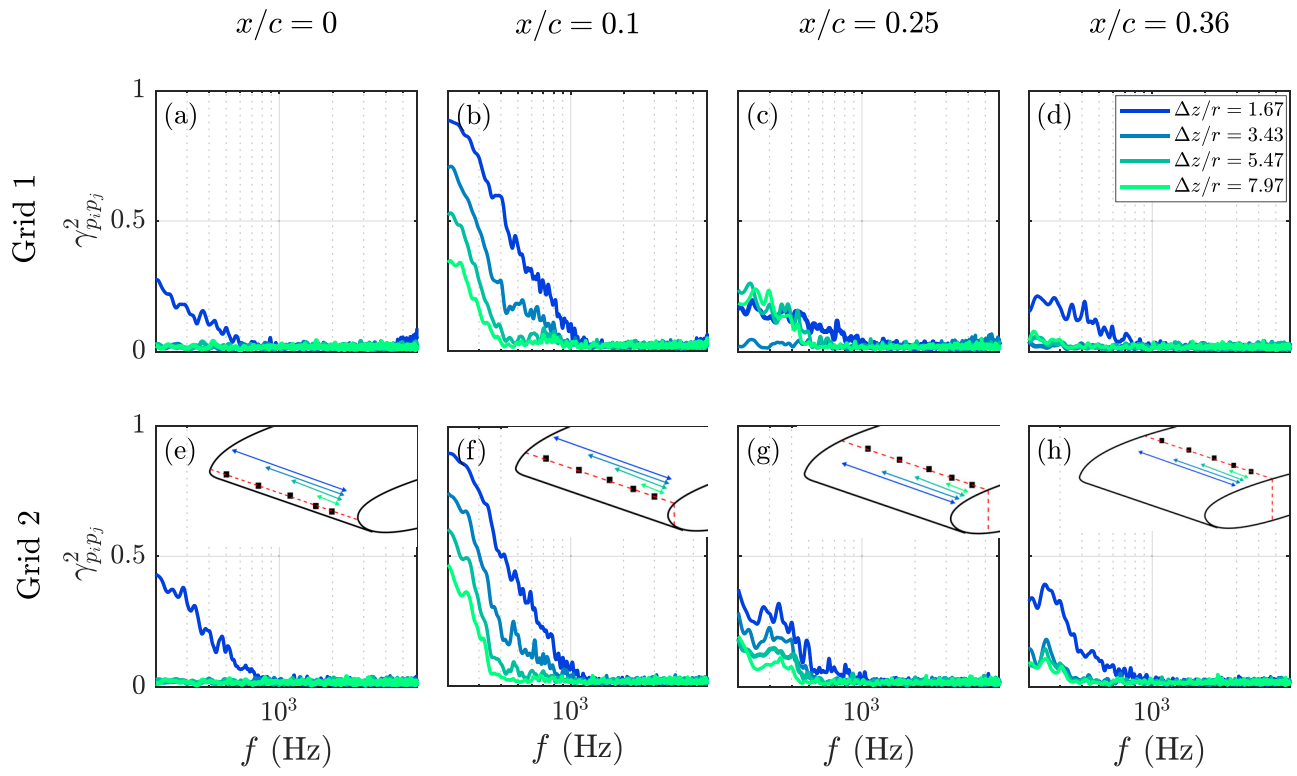

FIG. 14. Spanwise magnitude-square coherence ($\gamma^2_{p_i p_j}$) of surface pressure fluctuation measured between remote sensors with four spanwise separations ($\Delta z/r$) for (a) and (e) $x/c = 0$, (b) and (f) $x/c = 0.1$, (c) and (g) $x/c = 0.25$ and (c) and (g) $x/c = 0.36$ where the top row is the airfoil response to the flow generated by grid 1, and the bottom row is grid 2.

Further downstream, at $x/c = 0.25$ and $x/c = 0.36$, the pronounced difference of the spanwise pressure coherence levels between cases indicates an increased level of dependency to the turbulent inflow characteristics. In more detail, the level of spanwise coherence at the stagnation point, presented in Figs. 14(a) and 14(e), appear to be representative of inflow turbulence, as the larger structures of grid 2 generate a stronger low-frequency spanwise coherence. The highest level of coherence is observed at $x/c = 0.1$, and unlike the stagnation point, is comparable for both turbulent inflows. The coherence results from both flows exhibit high magnitudes at low frequencies, which steadily decays up to $f = 1000$ Hz. The highest coherence level, observed at the closest spanwise separation distance, i.e., $z/r = 1.67$, has a monotonic decrease with an increase in the separation distance. As the flow develops over the airfoil, the spanwise pressure coherence results at locations $x/c = 0.25$ and $x/c = 0.36$ are respective of the length scale and turbulence intensity level of the associated turbulent inflow, i.e., higher coherence magnitudes are evident for the grid 2 case and lower for the grid 1 case. These observations are consistent with the results at the stagnation point (i.e., $x/c = 0$). Further to this, the frequency range of the high level of pressure coherence is consistent with the previously discussed velocity coherence along the stagnation line (Fig. 12). It should be noted that the frequency range of the elevated far-field noise results presented in Sec. III (Fig. 3) overlaps with the frequency range of the elevated spanwise coherence results.

A complementary analysis to the spanwise pressure coherence is the streamwise coherence of the surface pressure fluctuations, which may reveal the streamwise spatial extent of the flow structures and elaborate the link between the stagnation point pressure fluctuations to airfoil response over the rest of the chord. Figure 15 presents the contour map of the surface pressure fluctuation magnitude-squared coherence calculated between the reference transducers $p1$ ($x/c = 0$) and $p2$ ($x/c = 0.03$) to all downstream transducers for the flows generated by grid 1 [Figs. 15(a) and 15(b)] and grid 2 [Figs. 15(c) and 15(d)]. The most striking result to emerge from Fig. 15 is the pronounced effect of the turbulence characteristics on the streamwise coherence levels and the substantial change the streamwise pressure coherence experiences regarding its reference, i.e., the change from the stagnation point ($x/c = 0$, $p1$) to a slightly downstream location ($x/c = 0.03$, $p2$). Comparing the streamwise pressure coherence results obtained with respect to the reference point $p1$, a higher level of coherence to the downstream transducers is evident for the flow generated by grid 1. However, even though the coherence levels are lower for the grid 2 case, it persists further downstream on the airfoil over a broader range of frequencies when compared to the result of the grid 1 case. Furthermore, the results also display that the peak coherence frequency decreases for both cases as the separation distance between the transducers increases. Considering the results with respect to the second reference location, $x/c = 0.03$ [$p2$, Figs. 15(b) and 15(d)], for both grid 1 and grid 2 cases, substantially increased coherence levels

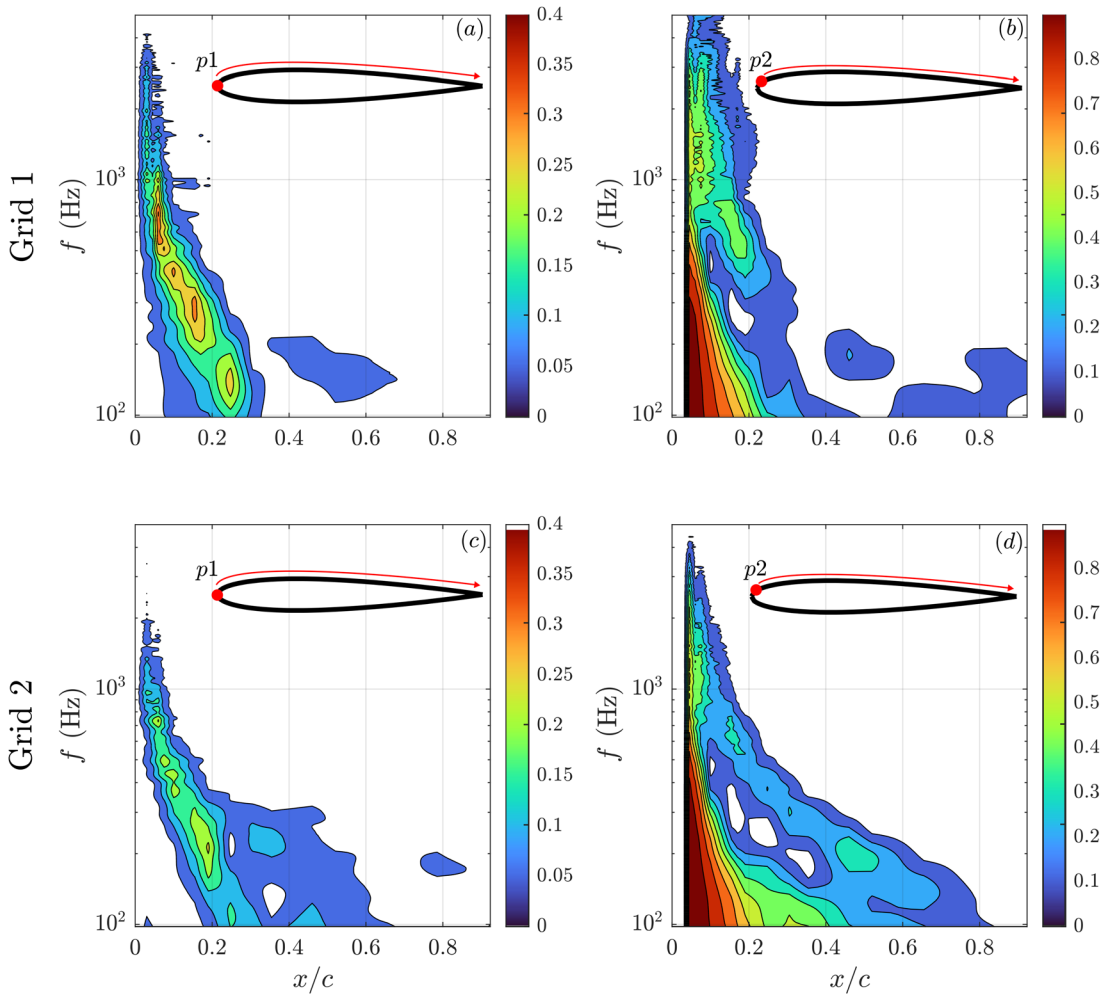

FIG. 15. Streamwise magnitude-square coherence ($\gamma^2_{p_ip_j}$) of surface pressure fluctuation measured between remote sensors along the chord of the airfoil for (a) and (c) transducer p1 located at $x/c = 0$ to downstream transducers *p*2–*p*18, and (b) and (d) transducer *p*2 located at $x/c = 0.03$ to downstream transducers p3–p18 for grid 1 (top row) and grid 2 (bottom row).

are displayed, especially with the transducers located in the vicinity of the reference transducer. At this location, there appear to be two main streamwise pressure coherence trends in the results of both cases, a significant low-frequency coherence between $100 < f < 600$ Hz, which rapidly decays with downstream distance, and a secondary coherence region, initially centered between $1000 < f < 2000$ Hz at $0.03 < x/c < 0.045$. In addition, in the case of grid 1, the streamwise pressure coherence results display a reduced level of dependency on the streamwise separation distance between $1000 < f < 2000$ Hz, where the coherence level varies in the narrowband between $0.4 < \gamma^2_{p_ip_j} < 0.6$. For grid 2 case, however, the streamwise pressure coherence level range is almost doubled, i.e., $0.2 < \gamma^2_{p_ip_j} < 0.6$, and the footprint of the structures interacting with the leading edge is felt much further downstream.

VII. PRESSURE–VELOCITY COHERENCE

Having examined the spanwise velocity coherence and both the spanwise and streamwise pressure coherence, we can garner more information by assessing the coherence between the velocity fluctuations along the stagnation line and the pressure fluctuations over the surface of the airfoil. The velocity–pressure coherence analyses may help us to characterize the spatial and temporal evolution of the coherent structures of the turbulent inflow and how they interact with the airfoil body. A single-wire hot-wire probe was utilized for velocity fluctuation measurement along the stagnation line between $-4.74 < x/r < -0.01$ while the pressure fluctuations were simultaneously sampled for all transducers on the airfoil. The coherence between the pressure and the velocity signals can be found from

$$\gamma^2_{p_iu_j}(f, \Delta x) = \frac{|\phi_{p_iu_j}(f)^2|}{|\phi_{p_ip_i}(f)||\phi_{u_ju_j}(f)|}, \tag{3}$$

where $\phi_{p_iu_j}(f)$ denotes the cross-power spectral density function calculated between the velocity and pressure signals, and Δx is the distance between the single-wire probe and the pressure transducer on the airfoil located at x_i and x_j, respectively.

Figure 16 displays the pressure–velocity coherence (p–u coherence) between the velocity fluctuations measured at $x/r = -4.74$ and $x/r = -0.01$ on the stagnation line to the pressure fluctuation measured at the front half-chord of the airfoil ($0 < x/c < 0.5$) for grid 1 (top row) and grid 2 (bottom row). Figure couples [Figs. 16(a) and 16(c), and 16(b) and 16(d)] show the p–u coherence results for velocity probe located at $x/r = -4.74$ and $x/r = -0.01$, respectively. A schematic illustrating the velocity measurement locations with an arrow indicating the array of pressure transducers along the chord is placed at the top row to ease the interpretation of the results. Consistent with the previous discussions on the coherence results (spanwise velocity coherence and streamwise and spanwise coherence of the pressure fluctuations), the frequency range of elevated pressure–velocity coherence is concurrent with the frequency range of the elevated turbulence interaction noise as presented in Fig. 3. Figure 16 provides an insight into how the airfoil surface pressure response is linked to the flow at two upstream locations along the stagnation line. The results show a high p–u coherence at low frequencies for grid 1 case, which indicates a close association of the pressure at p1, the stagnation point, to the velocity fluctuations at $x/r = -4.74$ as presented in Fig. 15(a). A secondary but weaker coherence region is evident over the chordwise region $0.05 < x/c < 0.3$. The spatial extent and distance to the leading edge of this secondary coherence island reduce as the frequency increases. In the case of grid 2, p–u coherence demonstrates a similar behavior to the upstream location ($x/r = -4.74$), as presented in Fig. 16(c). However, at the stagnation point over the airfoil, a lower p–u coherence is evident compared to that of grid 1 results. Furthermore, the secondary coherence island spreads until $x/c = 0.5$ for low frequencies. The p–u coherence between the stagnation point velocity ($x/r = -0.01$) and the pressure transducers over the airfoil is presented in Figs. 16(b) and 16(d). The p–u coherence appears to peak at low frequencies and are evident for the chordwise region of $0.03 < x/c < 0.4$ for grid 1 and $0.03 < x/c < 0.5$ for grid 2. In the case of grid 2, the p–u coherence is significantly higher over a broader frequency range with an extended spatial range compared to the results of the grid 1 case. A further inspection of Fig. 16 reveals some

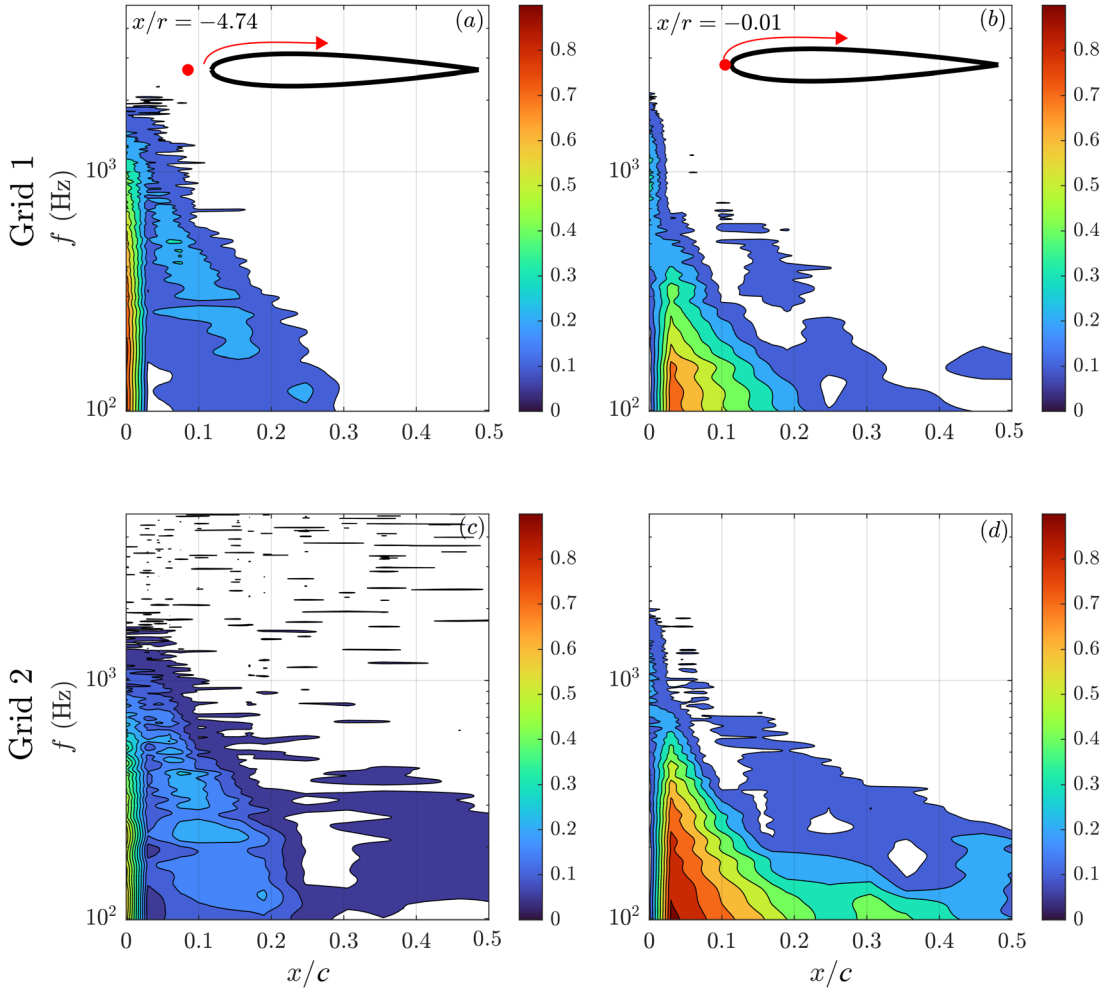

FIG. 16. Pressure–velocity magnitude-square coherence ($\gamma^2_{p_i u_j}$) for grid 1 (top row) and grid 2 (bottom row), (a) and (c) $\gamma^2_{p_i u_j}$ between the hot-wire probe located at $x/r = -4.74$ to pressure transducers between $0 < x/c < 0.5$, (b) and (d) $\gamma^2_{p_i u_j}$ between hot-wire probe located at $x/r = -0.01$ to pressure transducers between $0 < x/c < 0.5$.

resemblance to the streamwise pressure coherence results [Fig. 15, particularly for Figs. 15(b) and 15(d)], which corroborate the understanding of the relation between the velocity at the vicinity of the stagnation point and the airfoil surface pressure response.

In order to obtain a complete picture, Fig. 17 displays the coherence between the velocity fluctuations measured along the stagnation line ($0 < x/r < -3$) to the surface pressure fluctuations measured at two points on the airfoil $x/c = 0$ [Figs. 17(a) and 17(c)] and $x/c = 0.03$ [Figs. 17(b) and 17(d)], for both turbulent inflows generated by grid 1 (top row) and grid 2 (bottom row). A schematics of the reference pressure transducers on the airfoil and the axis of velocity measurement is placed at the bottom row to ease interpretation of the results. At first glance, the p–u coherence results display a remarkable change between the two chordwise pressure measurement locations on the airfoil surface, in further corroboration with the streamwise pressure coherence results displayed in Fig. 15. Considering the p–u coherence between the velocity fluctuations along the stagnation line and the pressure fluctuations at the stagnation point ($x/c = 0, p1$), the highest level of coherence is observed to the furthest upstream location in the case of grid 1, as displayed in Fig. 17(a). Furthermore, the pressure–velocity coherence level is significantly higher for the flow generated by grid 1 when compared to the p–u coherence results obtained from the grid 2 as presented in Fig. 17(c). Moreover, the peak coherence level in the case of grid 2 is frequency-dependent, unlike grid 1 results, and mostly lies in between $-1 < x/r < -2$. As the flow approaches the stagnation point, the low-frequency content of the coherence is reduced for both cases. However, the reduction behavior of the low-frequency coherence alters between the two cases. The p–u coherence for the flow generated by grid 1 appears to drop monotonically, approaching the stagnation point. In contrast, for the flow from grid 2, an abrupt drop of p–u coherence is evident between $0.33 < x/c < 0.96$, which corresponds approximately the region of

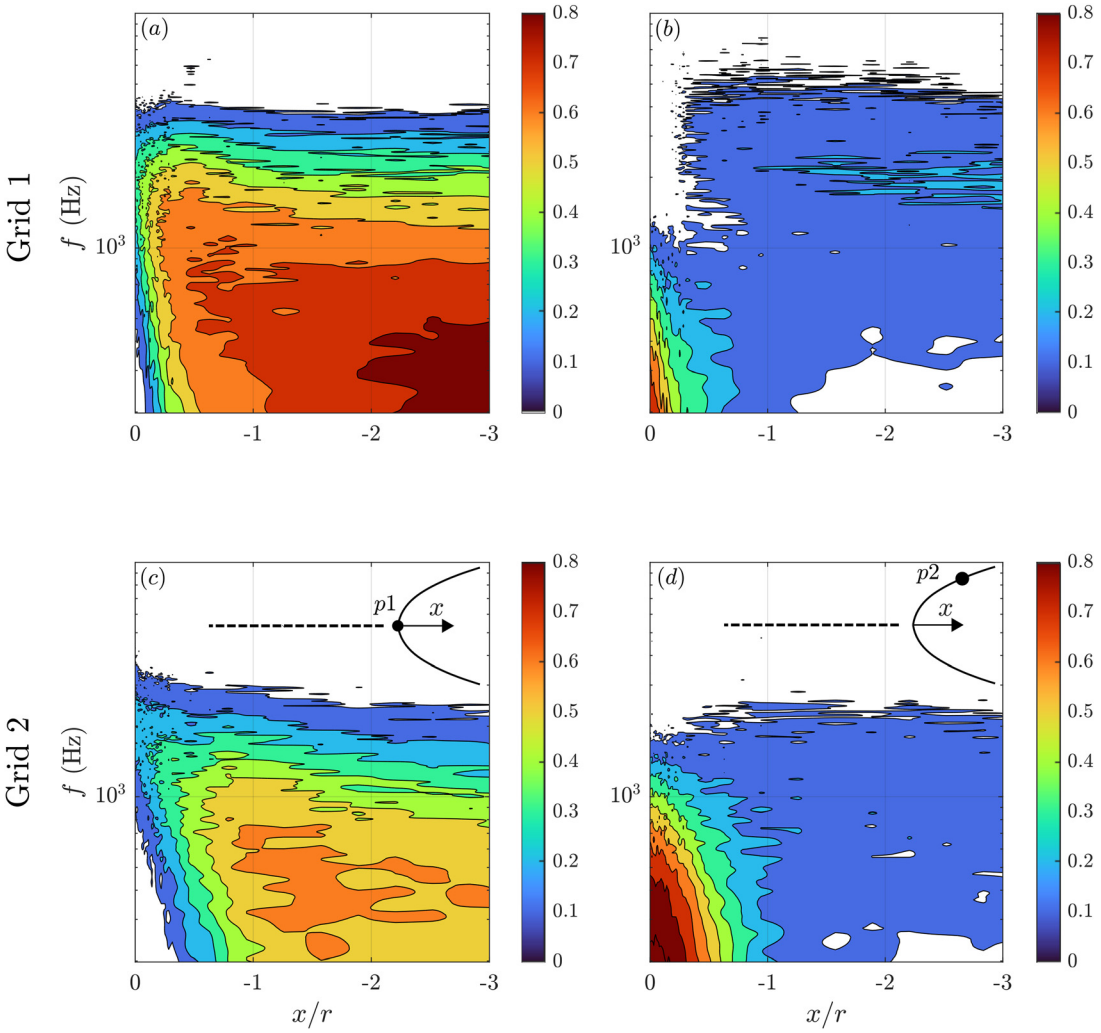

FIG. 17. Pressure–velocity magnitude-square coherence ($\gamma^2_{p_i u_j}$) for grid 1 (top row) and grid 2 (bottom row), (a) and (c) $\gamma^2_{p_i u_j}$ between pressure transducer p1 located at $x/c = 0$ to upstream measurement locations of hot-wire probe between $0 < x/r < -3$ and, (b) and (d) $\gamma^2_{p_i u_j}$ between pressure transducer p2 located at $x/c = 0.03$ to upstream measurement locations of hot-wire probe between $0 < x/r < -3$.

the lowest energy content region (Fig. 5) and smallest timescale (Fig. 10) in the velocity fluctuation. At the second chordwise position, $x/c = 0.03$, the p–u coherence behavior completely flips. The pressure–velocity coherence peaks at the closest velocity measurement point to the stagnation point ($x/r = -0.01$) and reduces as the separation distances increases. The p–u coherence levels are significantly higher for the grid 2 case over a broader frequency range and for larger separation distances between the velocity probe and the pressure transducer compared to the results of the grid 1 case. Overall, the p–u coherence results for the chordwise position $x/c = 0.03$ are respective of the incoming turbulent flow with a counter-intuitive behavior at the stagnation point. The presented data indicate that the characteristics of the stagnation point are sensitive to the incoming flow far upstream, and as the velocity measurement location approaches the stagnation point, the communication between the pressure transducer at the stagnation point and velocity probe. The loss of communication could be due to the redistribution of the energy from the streamwise component of the velocity to the crosswise or upwash component. Furthermore, it is worthwhile to note the pressure fluctuations over the airfoil have a strong connection to the velocity fluctuations in the vicinity of the stagnation point.

VIII. NEAR-FIELD TO FAR-FIELD PRESSURE COHERENCE

After discussing the pressure and velocity coherence results, it is now useful to address the relation between the surface pressure fluctuations over the airfoil to the far-field noise in detail. The near-field to far-field coherence is calculated by using Eq. (2), where the pressure fluctuations are obtained from the surface pressure transducers and far-field microphone array. Figure 18 shows the near-field to far-field pressure coherence between all the near-field pressure measurement locations over the entire chord of the airfoil to the far-field microphone at $\theta = 90°$, positioned directly above the leading edge of the airfoil. The top and bottom rows of Fig. 18 display the results of the flow generated by grid 1 (with turbulence intensity of 4.8% and an integral length scale of 5.9 mm) and grid 2 (with turbulence intensity of 10.1% and integral length scale of $\Lambda_x = 10.8$ mm), respectively. Figure couples [Figs. 18(a) and 18(d), 18(b) and 18(e), and 18(c) and 18(f)] are displaying the results associated with the surface sensors p1–p7, p8–p12, and p13–p18, respectively. A color is assigned to each transducer on the airfoil surface to ease the interpretation of the results, and the associated coherence curve is presented accordingly. Depicted in the figure, the level of near-field to far-field increases from near-zero values at the stagnation point to elevated values over the leading edge of the airfoil, which then reduces around the trailing edge for both grid 1 and grid 2 cases.

Furthermore, the frequency range of the highest near-field to far-field pressure coherence coincides with the frequency range of the observed turbulence interaction noise (see Fig. 3). Comparing the coherence levels of grid 1 case to grid 2 case, a pronounced decrease is evident for the entire measurement locations over the chord. This is an expected result due to the high levels of far-field noise and surface

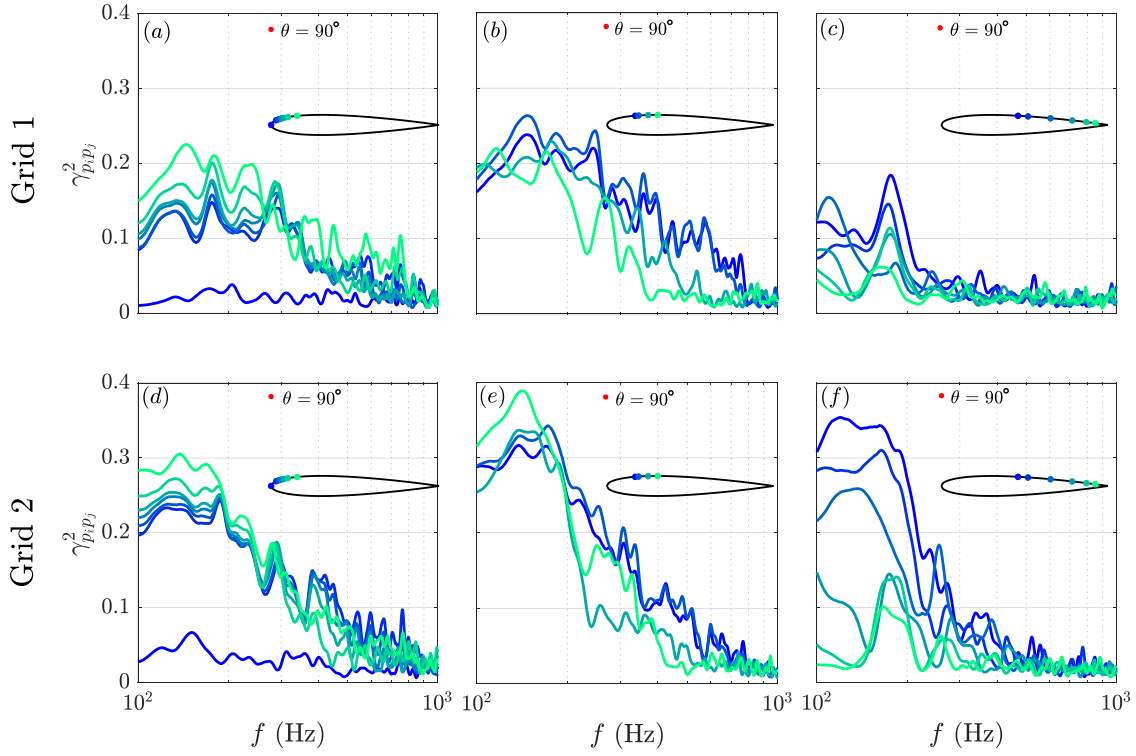

FIG. 18. Near-field to far-field magnitude-square coherence ($\gamma^2_{p_i p_j}$) between the surface pressure fluctuations to the far-field noise measured at $\theta = 90°$ for two turbulent inflows produced by grid 1 (top row) and grid 2 (bottom row) where (a) and (d) are transducers $p1$–$p7$ ($0 < x/c < 0.16$), (b) and (e) are transducers $p8$–$p12$ ($0.17 < x/c < 0.35$), and (c) and (f) are transducers $p13$–$p18$ ($0.46 < x/c < 0.92$).

pressure fluctuations observed and discussed in Figs. 3 and 13, respectively. Furthermore, considering the results for the grid 2 case, the chordwise region where coherence to the far-field exhibits elevated results extends up to $x/c = 0.7$. In both cases, the near-field to far-field coherence is most significant over the region of $0.17 < x/c < 0.35$ [Figs. 18(b) and 18(e)], which then reduces toward the trailing edge. For the results of the flow generated by grid 2, the high levels of near-field to far-field pressure coherence is sustained along the chord up to $x/c = 0.52$. It is worth noting that the stagnation point appears to be the only location on the airfoil that exhibits no discernible coherence to the far-field for both cases. From this observation, it is possible to deduce that although the incoming flow dictates the flow behavior of the stagnation point, it may be the rest of the airfoil response that radiates the sound to the far-field. Furthermore, the spatially persistent and increased near-field to far-field coherence level along the chord of the airfoil for the grid 2 case, the flow with the larger Λ_x and higher turbulence intensity may be associated with the increased far-field noise levels.

An assessment of the directivity of the near-field to far-field coherence may help us explore the details about the preferred propagation direction of the unsteady surface pressure fluctuations to far-field when exposed to different inflow conditions generated by grid 1 and grid 2. Figure 19 presents the magnitude squared coherence results calculated between the surface pressure fluctuations at transducer locations p2, p5, p9, and p13 on the airfoil to the microphones on the far-field array ($40° < \theta < 150°$) for the flows generated by grid 1 (top row) and grid 2 (bottom row). To ease the interpretation of the results, a color is assigned to each microphone on the far-field array and the associated coherence curve regarding the microphone is presented accordingly. A general inspection of the results reveals that coherence levels are significantly higher for the grid 2 case compared to grid 1, irrespective of the transducer location on the airfoil surface, which is consistent with the results of the preceding Fig. 18. A closer examination of the grid 1 results show that the coherence level is almost always lower for high polar angles. Furthermore, the difference between the coherence values peaks at lower frequencies. Another important observation is the gradual increase in overall coherence levels up to p9, after which a decrease in coherence magnitude is evident. The reduction in the coherence to far-field is consistent for all the surface pressure measurement transducers until the trailing edge, which is not shown here for brevity. Comparing the results of grid 2 case with grid 1, the overall elevated coherence values peak around p9 location. Moreover, the elevated results for the coherence level is sustained for the transducers further downstream until p15 ($x/c = 0.655$). Another feature to be underlined is the more consistent coherence levels for the grid 2 results. This result may appear somewhat counterintuitive; however, considering the directivity of the OASPL [Fig. 3(b)], the large and small observer angles (θ) show different behaviors between the flows of grid 1 and grid 2.

IX. CONCLUSION

This study presents an in-depth experimental investigation to address the effect of turbulence characteristics on the radiated interaction noise. Two passive grids were utilized to vary the turbulence characteristics of the flow, which enables a detailed examination of the airfoil interaction phenomenon with larger and smaller coherent structures in the flow in conjunction with the radiated noise.

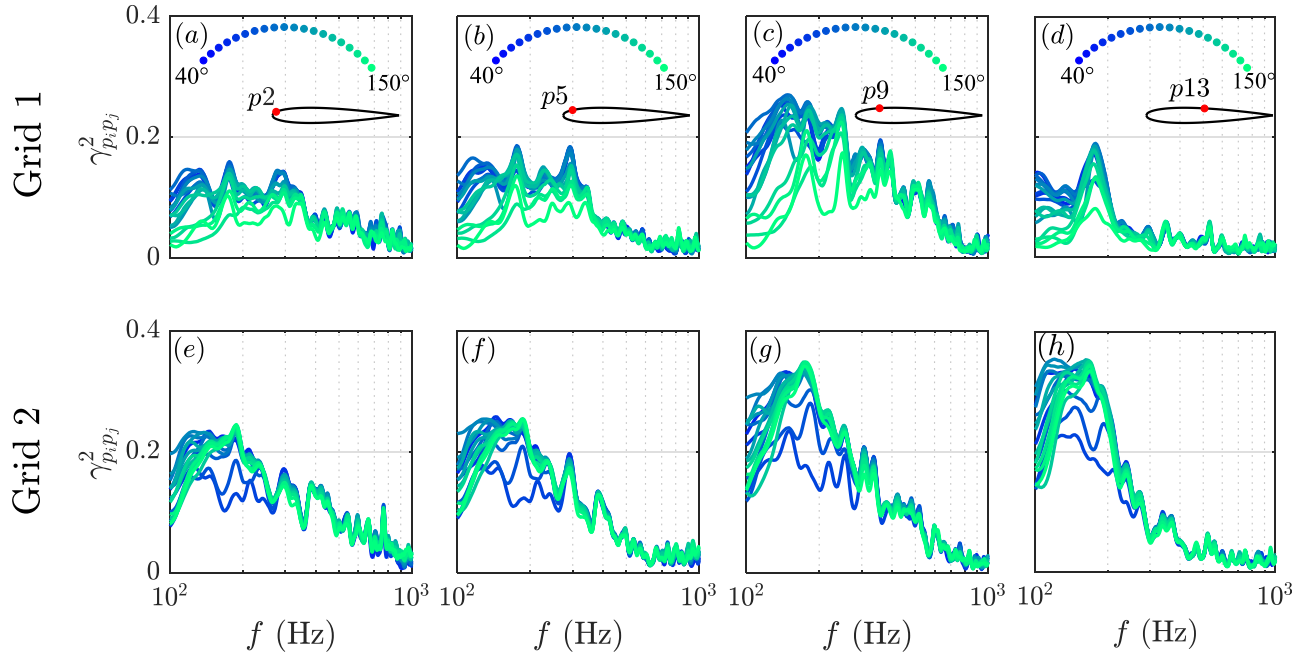

FIG. 19. Near-field to far-field magnitude-square coherence ($\gamma^2_{p_i p_j}$) between the surface pressure fluctuations and the far-field noise measured from the microphone array for polar angles $40° < \theta < 150°$ for two turbulent inflows produced by grid 1 (top row) and grid 2 (bottom row) for (a) and (e) $p2$ ($x/c = 0.03$) to far-field array, (b) and (f) $p5$ ($x/c = 0.08$) to far-field array, (c) and (g) $p9$ ($x/c = 0.19$) to far-field array, and (c) and (g) $p13$ ($x/c = 0.46$) to far-field array.

Far-field noise results showed that turbulence interaction noise significantly increases with increased in the turbulence intensity and integral length scale of the flow structures. The associated flow field is studied by steady pressure measurement, unsteady pressure measurements and velocity measurements. Mean-pressure coefficient results over the airfoil demonstrated that the inflow conditions, i.e., laminar and two turbulent inflows, do not affect the mean pressure distribution, yet there is some sensitivity to the root mean square of the pressure coefficient results. Analysis of the velocity measurements obtained along the stagnation line demonstrated that flow with higher turbulence intensity and a larger integral length scale significantly reduces the r.m.s. velocity fluctuations and the subsequent recovery in the proximity to the leading edge. Skewness and kurtosis analysis of the velocity fluctuation hints at a change in the nature of turbulence interaction. Results reveal a significant positive skewing of the velocity fluctuations, coupled with an increased kurtosis for the flow where the turbulence intensity is higher, and the flow structures are larger compared to the leading edge radius. There is no significant change to either skewness or kurtosis when the integral length scale of flow structures is comparable to the leading edge radius. A closer examination of the approaching flow with the two-point velocity coherence measurements along the stagnation line revealed that the flow structures of the size comparable to the leading edge radius are broken up, whereas flow structures with larger sizes distort and become more two-dimensional.

The airfoil surface pressure response demonstrated increased energy levels for surface pressure fluctuation spectra over a larger extent of the leading edge for the flow with larger structures and increased turbulence intensity. Interestingly, both cases showed a high spanwise pressure coherence at $x/c = 0.1$. The pressure–velocity coherence results suggest that the airfoil response is mainly influenced by the characteristics of the flow in the proximity of the stagnation point, whereas the flow characteristics at the stagnation point are associated with the flow further upstream. Finally, near-field to-far-field coherence analysis exhibits no discernible connection between the stagnation point and the radiated far-field noise. In contrast, the leading edge as a region is identified as the primary contributor to the radiated far-field noise. Moreover, the near-field to far-field coherence peaks around the thickest part of the airfoil and persists over a larger extent of the airfoil chord for the inflow condition with larger turbulence structures.

ACKNOWLEDGMENTS

The first author (L.B.) would like to acknowledge the financial support of Embraer S.A. and an Engineering and Physical Sciences Research Council doctoral training partnership (EPSRC DTP). The second author (A.C.) was sponsored by EPSRC via Grant No. EP/S013024/1 at the University of Bristol from 1/6/2020 to 1/12/2021. All authors would like to acknowledge the financial support of EPSRC via Grant No. EP/S013024/1.

AUTHOR DECLARATIONS

Conflict of Interest

The authors have no conflicts to disclose.

Author Contributions

Luke Bowen: Conceptualization (equal); Data curation (equal); Formal analysis (equal); Investigation (equal); Methodology (equal); Visualization (lead); Writing – original draft (lead); Writing – review & editing (lead). **Alper Celik:** Conceptualization (equal); Data curation (equal); Formal analysis (equal); Investigation (equal); Methodology (equal); Supervision (supporting); Visualization (supporting); Writing – original draft (supporting); Writing – review & editing (equal). **Mahdi Azarpeyvand:** Conceptualization (equal); Funding acquisition (lead); Supervision (lead); Writing – review & editing (equal).

DATA AVAILABILITY

The data that support the findings of this study are available from the corresponding author upon reasonable request.

REFERENCES

[1]L. F. G. Simmons, C. Salter, and G. I. Taylor, "Experimental investigation and analysis of the velocity variations in turbulent flow," Proc. R. Soc. London, Ser. A **145**, 212–234 (1934).
[2]G. K. Batchelor, A. A. Townsend, and G. I. Taylor, "Decay of vorticity in isotropic turbulence," Proc. R. Soc. London, Ser. A **190**, 534–550 (1947).
[3]G. Comte-Bellot and S. Corrsin, "The use of a contraction to improve the isotropy of grid-generated turbulence," J. Fluid Mech. **25**, 657–682 (1966).
[4]M. S. Uberoi and S. Wallis, "Effect of grid geometry on turbulence decay," Phys. Fluids **10**, 1216–1224 (1967).
[5]P. Roach, "The generation of nearly isotropic turbulence by means of grids," Int. J. Heat Fluid Flow **8**, 82–92 (1987).
[6]T. Kurian and J. H. M. Fransson, "Grid-generated turbulence revisited," Fluid Dyn. Res. **41**, 021403 (2009).
[7]L. Bowen, A. Celik, M. Azarpeyvand, and C. R. I. da Silva, "Grid generated turbulence for aeroacoustic facility," AIAA J. **60**, 1833–1847 (2022).
[8]T. F. Geyer, W. Poppe, and E. Sarradj, "Measurement of flow noise generation and pressure loss of nets and screens," Appl. Acoust. **134**, 69–74 (2018).
[9]P. F. Mish and W. J. Devenport, "An experimental investigation of unsteady surface pressure on an airfoil in turbulence. I. Effects of mean loading," J. Sound Vib. **296**, 417–446 (2006).
[10]T. Von Kármán and W. R. Sears, "Airfoil theory for non-uniform motion," J. Aeronaut. Sci. **5**, 379–390 (1938).
[11]W. R. Sears, "Some aspects of non-stationary airfoil theory and its practical application," J. Aeronaut. Sci. **8**, 104–108 (1941).
[12]J. M. R. Graham, "Similarity rules for thin aerofoils in non-stationary subsonic flows," J. Fluid Mech. **43**, 753–766 (1970).
[13]E. Reissner, "On the application of Mathieu functions in the theory of subsonic compressible flow past oscillating airfoils," Technical Report No. NACA 2363 (1951).
[14]C. Osborne, "Unsteady thin-airfoil theory for subsonic flow," AIAA J. **11**, 205–209 (1973).
[15]R. Amiet, "Compressibility effects in unsteady thin-airfoil theory," AIAA J. **12**, 252–255 (1974).
[16]J. J. Adamczyk, "Passage of a swept airfoil through an oblique gust," J. Aircr. **11**, 281–287 (1974).
[17]J. Adamczyk and R. Brand, "Scattering of sound by an aerofoil of finite span in a compressible stream," J. Sound Vib. **25**, 139–156 (1972).
[18]R. Amiet, "Acoustic radiation from an airfoil in a turbulent stream," J. Sound Vib. **41**, 407–420 (1975).
[19]J. C. R. Hunt, "A theory of turbulent flow round two-dimensional bluff bodies," J. Fluid Mech. **61**, 625–706 (1973).
[20]M. E. Goldstein and H. Atassi, "A complete second-order theory for the unsteady flow about an airfoil due to a periodic gust," J. Fluid Mech. **74**, 741–765 (1976).
[21]P. McKeough, "Effects of turbulence on aerofoils at high incidence," Ph.D. thesis (University of London, 1976).
[22]P. Mckeough and J. Graham, "The effect of mean loading on the fluctuating loads induced on aerofoils by a turbulent stream," Aeronaut. Q. **31**, 56–69 (1980).
[23]N. Curle and M. J. Lighthill, "The influence of solid boundaries upon aerodynamic sound," Proc. R. Soc. London, Ser. A **231**, 505–514 (1955).

[24]R. W. Paterson and R. K. Amiet, "Noise and surface pressure response of an airfoil to incident turbulence," J. Aircr. **14**, 729–736 (1977).
[25]P. Migliore and S. Oerlemans, "Wind tunnel aeroacoustic tests of six airfoils for use on small wind turbines," J. Sol. Energy Eng. **126**, 974–985 (2004).
[26]J. Gershfeld, "Leading edge noise from thick foils in turbulent flows," J. Acoust. Soc. Am. **116**, 1416–1426 (2004).
[27]S. Moreau and M. Roger, "Effect of angle of attack and airfoil shape on turbulence-interaction noise," AIAA Paper No. 2005-2973, 2005.
[28]W. J. Devenport, J. K. Staubs, and S. A. Glegg, "Sound radiation from real airfoils in turbulence," J. Sound Vib. **329**, 3470–3483 (2010).
[29]A. Celik, L. Bowen, and M. Azarpeyvand, "Experimental investigation on the unsteady surface pressure fluctuation patterns over an airfoil," Phys. Fluids **34**, 105134 (2022).
[30]F. V. Hutcheson, T. F. Brooks, and D. J. Stead, "Measurement of the noise resulting from the interaction of turbulence with a lifting surface," Int. J. Aeroacoust. **11**, 675–700 (2012).
[31]J. Gill, X. Zhang, and P. Joseph, "Symmetric airfoil geometry effects on leading edge noise," J. Acoust. Soc. Am. **134**, 2669–2680 (2013).
[32]J. Christophe, "Application of hybrid methods to high frequency aeroacoustics," Ph.D. thesis (Université Libre de Bruxelles, 2011).
[33]L. D. Santana, J. Christophe, C. Schram, and W. Desmet, "A rapid distortion theory modified turbulence spectra for semi-analytical airfoil noise prediction," J. Sound Vib. **383**, 349–363 (2016).
[34]R. Zamponi, S. Satcunanathan, S. Moreau, D. Ragni, M. Meinke, W. Schröder, and C. Schram, "On the role of turbulence distortion on leading-edge noise reduction by means of porosity," J. Sound Vib. **485**, 115561 (2020).
[35]B. Lyu, M. Azarpeyvand, and S. Sinayoko, "Noise prediction for serrated leading-edges," AIAA Paper No. 2016-2740, 2016.
[36]B. Lyu and M. Azarpeyvand, "On the noise prediction for serrated leading edges," J. Fluid Mech. **826**, 205–234 (2017).
[37]J. Kim, S. Haeri, and P. Joseph, "On the reduction of aerofoil-turbulence interaction noise associated with wavy leading edges," J. Fluid Mech. **792**, 526–552 (2016).
[38]S. Narayanan, C. Paruchuri, S. Haeri, P. Joseph, J. W. Kim, and C. Polacsek, "Airfoil noise reductions through leading edge serrations," Phys. Fluids **27**, 025109 (2015).
[39]C. Paruchuri, P. Joseph, S. Narayanan, C. Vanderwel, J. Turner, J. W. Kim, and B. Ganapathisubramani, "Performance and mechanism of sinusoidal leading edge serrations for the reduction of turbulence-aerofoil interaction noise," J. Fluid Mech. **818**, 435–464 (2017).
[40]L. Bowen, A. Celik, B. Zhou, M. F. Westin, and M. Azarpeyvand, "The effect of leading edge porosity on airfoil turbulence interaction noise," J. Acoust. Soc. Am. **152**, 1437–1448 (2022).
[41]L. Bowen, A. Celik, M. Azarpeyvand, and C. R. da Silva, "Porous geometry effects on the generation of turbulence interaction noise," AIAA Paper No. 2021-2193, 2021.
[42]K. N. Chanaud and R. R. Sitterding, "Experiments on porous blades as a means of reducing fan noise," J. Acoust. Soc. Am. **59**, 564–575 (1976).
[43]T. Geyer, E. Sarradj, J. Giesler, and M. Hobracht, "Experimental assessment of the noise generated at the leading edge of porous airfoils using microphone array techniques," AIAA Paper No. 2011-2713, 2011.
[44]T. Geyer, E. Sarradj, and J. Giesler, "Application of a beamforming technique to the measurement of airfoil leading edge noise," Adv. Acoust. Vib. **2012**, 905461.
[45]E. Sarradj and T. Geyer, "Noise generation by porous airfoils," AIAA Paper No. 2007-3719, 2007.
[46]M. Roger, C. Schram, and L. D. Santana, "Reduction of airfoil turbulence-impingement noise by means of leading-edge serrations and/or porous material," AIAA Paper No. 2013-2108, 2013.
[47]Y. D. Mayer, B. Zang, and M. Azarpeyvand, "Near-field aeroacoustic characteristics of a stalled NACA 0012 aerofoil," in *Proceedings of the 23rd International Congress on Acoustics: Integrating 4th EAA Euroregio*, 9–13 September (Deutsche Gesellschaft für Akustik, Aachen, Germany, 2019), pp. 5383–5390.
[48]A. P. G. Sagrado, "Boundary layer and trailing edge noise sources," Ph.D. thesis (University of Cambridge, 2008).
[49]Y. D. Mayer, H. K. Jawahar, M. Szöke, S. A. S. Ali, and M. Azarpeyvand, "Design and performance of an aeroacoustic wind tunnel facility at the university of bristol," Appl. Acoust. **155**, 358–370 (2019).
[50]P. Welch, "The use of fast Fourier transform for the estimation of power spectra: A method based on time averaging over short, modified periodograms," IEEE Trans. Audio Electroacoust. **15**, 70–73 (1967).
[51]L. Bowen, A. Celik, M. Azarpeyvand, and C. R. I. da Silva, "On the use of tailored permeable surfaces for turbulence interaction noise control," AIAA Paper No. 2020-2530, 2020.
[52]J. Hinze, *Turbulence* (McGraw-Hill, 1975).
[53]Z. Harun, J. P. Monty, R. Mathis, and I. Marusic, "Pressure gradient effects on the large-scale structure of turbulent boundary layers," J. Fluid Mech. **715**, 477–498 (2013).
[54]J. Isaza, R. Salazar, and Z. Warhaft, "On grid-generated turbulence in the near- and far field regions," J. Fluid Mech. **753**, 402–426 (2014).
[55]S. Glegg and W. Devenport, *Aeroacoustics of Low Mach Number Flows: Fundamentals, Analysis, and Measurement* (Academic Press, 2017).